Flight Dynamics Modeling of Coaxial Rotorcraft UAVs

49

Fei Wang, Jinqiang Cui, Ben M. Chen, and Tong H. Lee

Contents

Abstract

In many unmanned aerial vehicle (UAVs)-related engineering projects, flight dynamics modeling of the controlled platform usually forms the foundation of the whole project development. An accurate mathematical model of the controlled UAV not only makes high-performance model-based control law design possible but also provides insights into the mechanical design of the aerial platform so that radical improvements can be made at the beginning of the development. However, the topic of flight dynamics modeling is somehow not paid enough

F. Wang (✉) • J. Cui • B.M. Chen • T.H. Lee
Control and Simulation Lab, Department of Electrical and Computer Engineering, National University of Singapore, Singapore
e-mail: wangfei@nus.edu.sg; jinqiang@nus.edu.sg; bmchen@nus.edu.sg; eleleeth@nus.edu.sg

attention to across the general engineering audience. This chapter aims to disseminate the knowledge of systematic modeling of UAV flight dynamics by talking about UAV model formulation, parameter identification, and model verification. The methodology of UAV model formulation and parameter identification based on the case study of two kinds of coaxial helicopters will be explained. Modeling of coaxial helicopters, despite the common governing kinematic and dynamic principles, deserves special attention due to their distinctive mechanical structure and aerodynamics behavior. The modeling procedures and parameter identification process presented in this chapter also serve as a guideline for modeling other types of aerial vehicles.

49.1 Introduction

In recent years, unmanned aerial vehicles (UAVs) have been more actively involved in military and civil operations. Possible UAV applications include reconnaissance and intelligence gathering, forest patrol, coastline monitoring, and search and rescue (Tsach et al. 2010). In all kinds of UAV development, the flight dynamics modeling of the controlled platform always forms the cornerstone of the whole project. UAV modeling not only provides an accurate mathematical model so that advanced model-based control law design techniques can be used but also provides insights into the mechanical design of the aerial platform itself. Moreover, in contrast to those conventional manned aerial vehicles, UAV platforms are normally custom-made or largely modified from off-the-shelf products to cope with the payload requirement and the mounting geometry of the onboard avionics. UAV platforms may possess different working principles, ranging from fixed-wing, rotorcraft, flapping-wing to mono-copters like the Samurai (Rosen and Seter 1991). To model some of the special types of aerial platforms, the well-established work for the conventional aerial platforms in literature cannot be applied directly. Hence, it is especially useful to let UAV developers understand how the models are derived and how to identify unknown parameters embedded within the models.

Many works related to flight dynamics modeling and model-based parameter identification of aerial vehicles are conducted in literature. Some of them are done for the ultimate purpose of UAV development. In Heffley and Mnich (1988), a mathematical model for the conventional single-rotor helicopter with adequate complexity was derived, and the report highlighted the formulation of the main rotor thrust generation. In Johnson (1994), a fairly comprehensive and detailed coverage of helicopter working theory and design considerations were provided in aspects including helicopter vertical flight, forward flight, mathematics of rotating systems, rotary wing dynamics and aerodynamics, aeroelasticity, and stability and control. Based on the above works, Cai et al. (2012) obtained a comprehensive nonlinear model of a miniature single-rotor helicopter. This work has also later been extended in a book (Cai et al. 2011) with other UAV-related topics like UAV construction, software development, and controller design.

In more recent years, the development of UAV platforms has entered the era of miniature, microscale, and even nanoscale. The used-to-be efficient conventional fixed-wing or single-rotor helicopter structure may not be an optimum design anymore. The reduced form factor has also resulted in more innovative and unconventional aerodynamic designs, and for these new types of platforms, quite a few new modeling works have been published. In Nonami et al. (2010), the mathematical model of a miniature coaxial helicopter is derived in the transfer function form. The identified linear model is used for optimal controller design. In Bermes (2010), the design and dynamic modeling and the simulation of an autonomous coaxial micro helicopter platform (muFly) are investigated. A modular dynamic model is developed, which incorporates the active and passive flapping characteristics of a hingeless rotor system, the stabilizer bar dynamics, roll-pitch steering by swashplate or displacing center of mass, etc.

Coaxial helicopter is an attractive UAV platform due to its small dimension, high thrust-to-weight ratio, and aerodynamic symmetry. If a coaxial helicopter and a single-rotor helicopter are of the same weight, the size of the coaxial helicopter can be 35–40 % smaller. In addition, the aerodynamic symmetry of coaxial helicopters successfully gets rid of the yaw moment and side forces commonly seen in single-rotor helicopters. Thus, the coaxial helicopter is much more effective in fast forward flights. These advantages make the coaxial helicopter ideal for UAV operation in confined environments such as indoor and cluttered outdoor. There are two types of coaxial helicopters. One has rotor blades with a fixed collective pitch, while the other is with variable collective pitch. In the following content of this chapter, they will be called the fixed-pitch coaxial and the variable-pitch coaxial in short. The dynamic modeling of these two kinds of coaxial helicopters will form the main discussion in this chapter.

A major difference of modeling between the coaxial helicopter and the conventional single-rotor helicopter is the pair of concentric rotors, in which each of them rotates with the induced velocity affected by the other. Such relationship is described in Colin (1997). Detailed studies of the wake dynamics of the two rotors were also documented in Kim and Brown (2006), Rand and Khromov (2010), and Lim et al. (2009). Another specialty of coaxial helicopter is the stabilizer bar attached to the top rotor hub, which passively stabilizes the helicopter. It, however, causes strong influences to the rotor dynamics especially to the fixed-pitch coaxial configuration as the upper rotor is not linked to any servo. As a result, the cyclic pitch control of the upper rotor is solely induced by the stabilizer bar. The stabilizer bar dynamics is commonly modeled as a first-order lag system (Mukherjee and Waslander 2011). In the works shown in Mukherjee and Waslander (2011) and Schafroth et al. (2010), the tip-path-plane (TPP) dynamics is separated into the upper and lower portion, where only the lower TPP is controlled by the servo inputs.

In a few recent works on the modeling of miniature coaxial helicopter, although fairly complete nonlinear or linear models are obtained, the works lack intuitive explanation of the model formulation. Moreover, their methods of parameter identification are not comprehensive enough. For example, in Neamtu et al. (2010),

the helicopter dynamics were treated as a black box, while the whole system is vaguely identified using the CIFER (Comprehensive Identification from FrEquency Responses) toolkit. To complement the existing work, this book chapter presents the detailed derivation of the nonlinear model for both the fixed-pitch and the variable-pitch coaxial helicopters.

The content of this chapter is organized as follows: Sect. 49.2 briefly gives the working principles of both the fixed-pitch and the variable-pitch coaxial helicopters. Next, Sect. 49.3 will comprehensively formulate the coaxial flight dynamics system, starting from kinematics, rigid-body dynamics, and then force/torque composition and generation. Some parts of the model formulation can be shared by both types of coaxial helicopters, while the differences in rotor thrust generation and rotor flapping dynamics will be separately explained. Model-based parameter identification will be introduced in Sect. 49.4 with the fixed-pitch coaxial as an example. Last but not least, Sect. 49.5 will verify the derived model of the fixed-pitch coaxial case and proves the fidelity of the overall modeling methodology.

49.2 Working Principle of Coaxial Helicopters

Before any rigorous derivation of the flight dynamic models of the aforementioned two types of coaxial helicopters, the general working principles of the two will first be introduced so that it will be easier for readers to understand the later detailed model formulation. First of all, both platforms have a pair of contrarotating rotors (upper and lower) to provide the fundamental lift force for the overall platform. This is indeed where the term "coaxial" comes from.

For the fixed-pitch coaxial helicopter, as shown in Fig. 49.1, the collective pitch of the rotor blades cannot be changed. Hence, the heave and yaw motion of the platform can only be controlled by varying the rotational speed of the rotors, which are linked to two separate motors with step-down gears. In general, the summation of the motor speeds determines the helicopter vertical motion, while the difference of the two determines the yaw motion. Rolling and pitching are accomplished by introducing a cyclic pitch to the lower rotor via a dual-servo-controlled swashplate. In this way, a tilted flapping of the rotor blades can be induced, and the generated rotor thrust becomes non-vertical. In the case of the platform shown in Fig. 49.1, which is called the ESky Big Lama, the cyclic pitch of the upper rotor is not actively controlled. Instead, the rotor hub tethers together with a stabilizer bar. As the stabilizer bar is purposely constructed with relatively high moment of inertia, when the helicopter fuselage suddenly tilts, the stabilizer bar tends to remain rotating at the original level plane. This introduces a cyclic pitch to the upper rotor, and it is purposely designed in a way that the thrust tilting resulted from this cyclic pitch counters the instantaneous motion of the helicopter. Therefore, this kind of fixed-pitch coaxial helicopters is inherently stable with regard to their attitude angles.
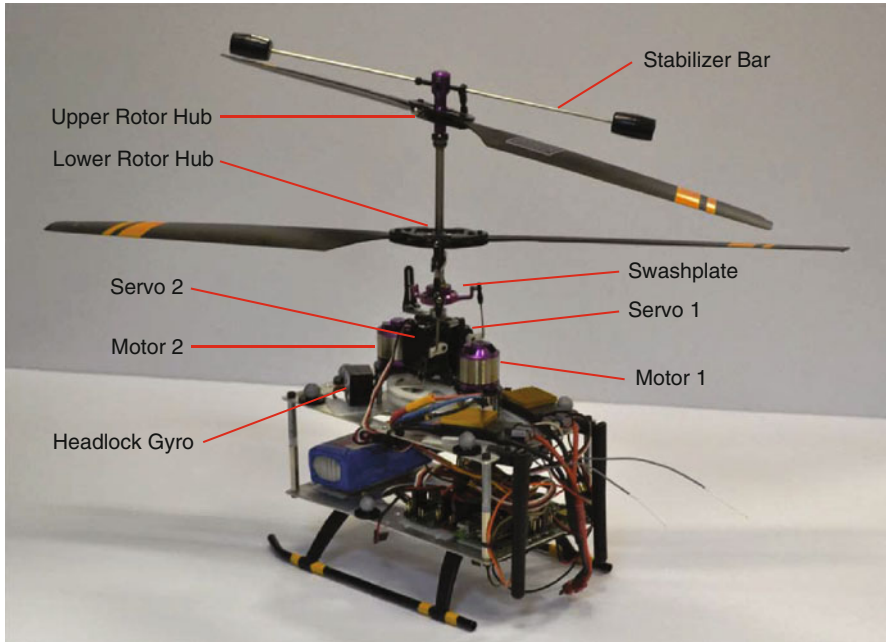
Fig. 49.1 Description of the fixed-pitch coaxial helicopter

On the other hand, the variable-pitch coaxial helicopter, as shown in Fig. 49.2, is a mini coaxial helicopter customized according to the design of full-scale coaxial helicopter from the Kamov design bureau. Its rotor head is equipped with integrated hinges and shock-resistant dampers. This helicopter also consists of two contrarotating rotors. However, unlike the fixed-pitch coaxial, the rotational speeds of the variable-pitch coaxial helicopter's rotors are maintained at the same constant speed in normal flight conditions. The dynamic motion of the helicopter is achieved by actively changing the pitch angles of both upper and lower rotors via the upper swashplate and the lower swashplate, respectively. The pitch angles of both rotors are constituted by collective pitch and cyclic pitch, which are mixed controlled by three servos linked to the lower swashplate. The two swashplates are always parallel to each other since they are circumferentially connected by three rigid linkages. The upper rotor is attached with a Bell-Hiller stabilizer bar which introduces damping to the rotor's cyclic pitch. Collective and cyclic inputs from servos are transferred to the lower swashplate and also induced to the top swashplate, resulting in the dynamic movement of the helicopter in heave direction or pitch-roll direction. The yaw direction control is realized by changing the collective pitch angle of the lower rotor. For this particular platform, the upper rotor and lower rotor are driven by the same brushless direct current (DC) electric motor with the same gear ratio. Hence, the rotational speeds of the upper rotor and the lower rotor are always the same.
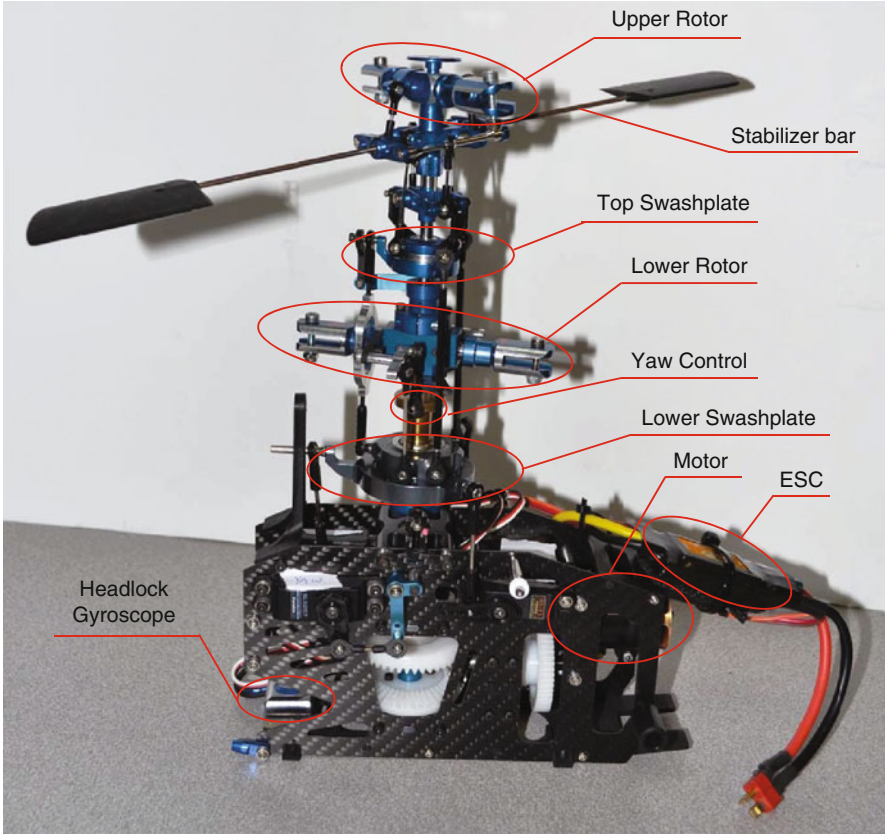
Fig. 49.2 Description of the variable-pitch coaxial helicopter

49.3 Model Formulation

49.3.1 Model Overview

The mathematical model of any continuous physical dynamic system can be expressed in the following compact form:

$$\dot{\mathbf{x}} = \mathbf{f}(\mathbf{x}, \mathbf{u}, \mathbf{w}), \tag{49.1}$$

where $\mathbf{x}$ is the state vector, $\mathbf{u}$ is the input vector, and $\mathbf{w}$ represents external disturbances. For the case of the fixed-pitch coaxial helicopter system, the system state and input vectors can be defined as

$$\mathbf{x} = (x\ y\ z\ u\ v\ w\ \phi\ \theta\ \psi\ p\ q\ r\ a_{\text{up}}\ b_{\text{up}}\ a_{\text{dw}}\ b_{\text{dw}}\ \Omega_{\text{up}}\ \Omega_{\text{dw}}\ r_{\text{fb}})^{\text{T}}, \tag{49.2}$$

Table 49.1 Physical meaning of state variables

Symbol	Physical meaning	Unit
x		
y	$\mathbf{p}$, position in the ground frame	m
z		
u		
v	$\mathbf{v}_b$, linear velocity in the body frame	m/s
w		
ϕ	Roll ⎫	
θ	Pitch ⎬ attitude angle	rad
ψ	Yaw ⎭	
p		
q	$\boldsymbol{\omega}$, angular velocity in body frame	rad/s
r		
a_{up}	Longitudinal ⎫ flapping angle of upper blades	rad
b_{up}	Lateral ⎭	
a_{dw}	Longitudinal ⎫ flapping angle of lower blades	rad
b_{dw}	Lateral ⎭	
Ω_{up}	Rotational speed of the upper rotor	
Ω_{dw}	Rotational speed of the lower rotor	
r_{fb}	Controller state of yaw stability augmentation	NA

$$\mathbf{u} = (\delta_{\mathrm{ail}} \ \delta_{\mathrm{ele}} \ \delta_{\mathrm{thr}} \ \delta_{\mathrm{rud}})^{\mathrm{T}}, \tag{49.3}$$

$$\mathbf{w} = (\omega_u \ \omega_v \ \omega_w)^{\mathrm{T}}. \tag{49.4}$$

For the case of the variable-pitch coaxial helicopter system, the system state and input vectors can be defined as

$$\mathbf{x} = (x \ y \ z \ u \ v \ w \ \phi \ \theta \ \psi \ p \ q \ r \ a_{\mathrm{up}} \ b_{\mathrm{up}} \ a_{\mathrm{dw}} \ b_{\mathrm{dw}} \ r_{\mathrm{fb}})^{\mathrm{T}}, \tag{49.5}$$

$$\mathbf{u} = (\delta_{\mathrm{ail}} \ \delta_{\mathrm{ele}} \ \delta_{\mathrm{thr}} \ \delta_{\mathrm{rud}})^{\mathrm{T}}, \tag{49.6}$$

$$\mathbf{w} = (\omega_u \ \omega_v \ \omega_w)^{\mathrm{T}}. \tag{49.7}$$

The physical meanings of the state, input, and disturbance variables are listed in Tables 49.1–49.3. It should be noted that the fixed-pitch coaxial helicopter has two additional state variables, Ω_{up} and Ω_{dw}, because its rotor rotational speeds keep changing during normal flights and its motor dynamics is not fast enough to be neglected. On the other hand, the rotors of the variable-pitch coaxial platform always rotate at the same speed. Thus, no dynamics need to be considered.

With regard to the input definition, the conventional radio-controlled (RC) joystick signals, aileron (δ_{ail}), elevator (δ_{ele}), throttle (δ_{thr}), and rudder (δ_{rud}), normalized to $[-1, 1]$ with respect to their corresponding minimum and maximum values, are chosen as the primary system inputs. This kind of input definition makes sure that the modeling methodology is also applicable to other types of

Table 49.2 Physical meaning of input variables

Variables	Physical meaning	Range
δ_{ail}	Control deflection for lateral cyclic pitch	$[-1, 1]$
δ_{ele}	Control deflection for longitudinal cyclic pitch	$[-1, 1]$
δ_{thr}	Control deflection for collective pitch	$[-1, 1]$
δ_{rud}	Control deflection for collective pitch of tail rotor	$[-1, 1]$
$\bar{\delta}_{rud}$	Control deflection for yaw-stability-augmentation controller	$[-1, 1]$

Table 49.3 Physical meaning of wind disturbance variables

Variables	Physical meaning
ω_u	Wind velocity in the helicopter x-axis
ω_v	Wind velocity in the helicopter y-axis
ω_w	Wind velocity in the helicopter z-axis

aerial platforms. Usually, the helicopter attitude angles (ϕ, θ), heading (ψ), and 3D position (x,y,z) are chosen to be the ultimate controlled outputs as they can comprehensively define the state of the helicopter in the full 6 degree-of-freedom (6DoF) space.

Furthermore, to derive a mathematical model of a complex system, it is preferable to modularize the overall system into subsystems so that the divide-and-conquer strategy can be used. Here, an overview of the two model structures is shown in Figs. 49.3 and 49.4. From the inputs to the state variables, there are numerous blocks representing all the subsystems involved. The two models share quite a few similarities but preserve their own distinctive features as well. On the one hand, the input and output definitions are unified for both, and the same kinematics and dynamics blocks can be used to relate the body-frame forces and moments to the helicopter 6DoF motion. On the other hand, the two models are different in the mechanism in generating the individual forces and moments. This results in two different sets of intermediate model blocks. In the following sections, mechanisms in all these blocks will be explained in detail. The similar blocks between these two types of platforms will be discussed together, while the different blocks will be discussed separately.

49.3.2 Kinematics and Rigid-Body Dynamics

As a common practice of aeronautic analysis, model formulation of a flying vehicle normally assumes that the target platform is a rigid body. Thus, it follows the universal 6DoF kinematics equations and the Newton-Euler dynamics equations. Two main coordinate frames are generally involved to link the equations. One is the north-east-down (NED) frame, and the other is the helicopter body frame. While the NED frame is stationary with respect to a static observer on the ground, the body
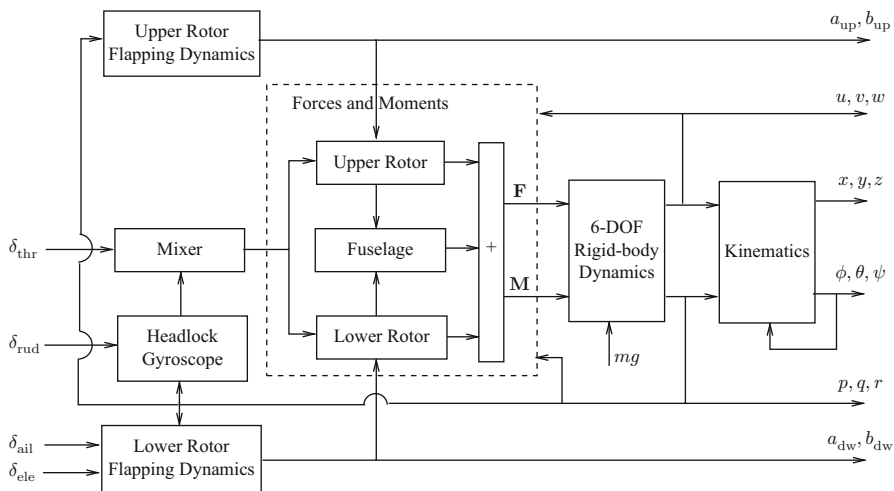
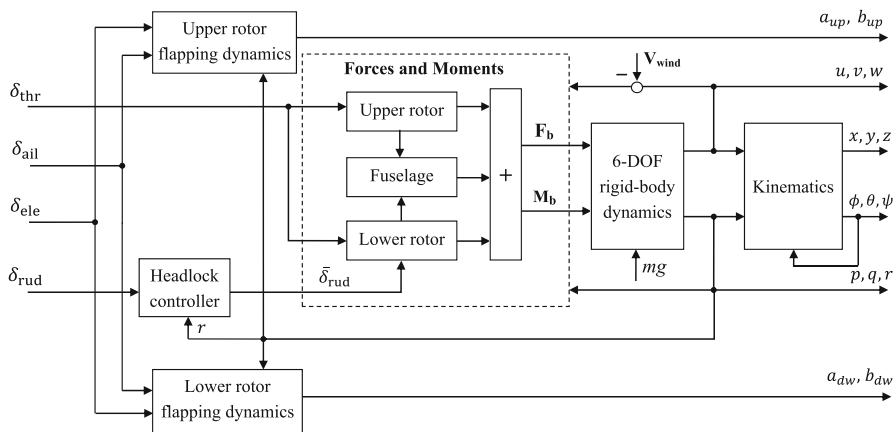**Fig. 49.3** Model structure of fixed-pitch coaxial helicopter

Fig. 49.4 Model structure of variable-pitch coaxial helicopter

frame is placed at the center of gravity (CG) of the coaxial helicopter, where its origin and orientation move together with the helicopter fuselage (see Fig. 49.5). It is worth noting that the listed formulas to describe the kinematics and dynamics of the coaxial helicopter are indeed universal to all other rigid-body vehicles.

The relationship between the helicopter NED-frame position and its body-frame velocity is determined by the following navigation equation:

$$
\begin{pmatrix} \dot{x} \\ \dot{y} \\ \dot{z} \end{pmatrix} = \begin{bmatrix} c_\psi c_\theta & c_\psi s_\theta s_\phi - s_\psi c_\phi & c_\psi s_\theta c_\phi + s_\psi s_\phi \\ s_\psi c_\theta & s_\psi s_\theta s_\phi + c_\psi c_\phi & s_\psi s_\theta c_\phi - c_\psi s_\phi \\ -s_\theta & c_\theta s_\phi & c_\theta c_\phi \end{bmatrix} \begin{pmatrix} u \\ v \\ w \end{pmatrix},
\tag{49.8}
$$

Fig. 49.5 Coordinate frames and various forces and torques
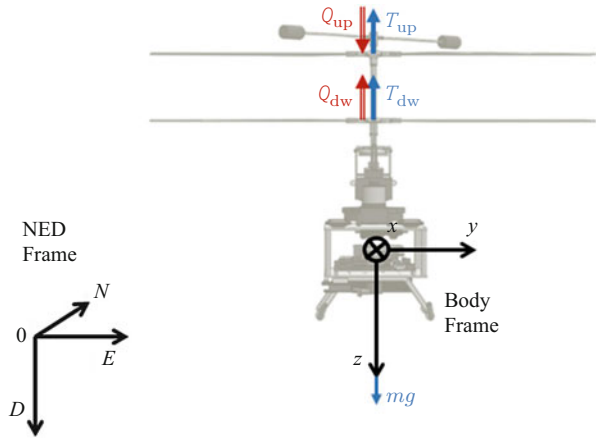
where x, y, z are the NED-frame position components of the helicopter and u, v, w are the body-frame velocity components. ϕ, θ, ψ are the conventional roll, pitch, yaw angles of the helicopter fuselage and s_*, c_* denote $\sin(*)$, $\cos(*)$, respectively. It is also critical to point out that the Euler angle derivatives, $\dot{\phi}$, $\dot{\theta}$, $\dot{\psi}$, are not orthogonal to each other. They are related to the body-frame angular rates, p, q, r, by the following equation:

$$\begin{pmatrix} \dot{\phi} \\ \dot{\theta} \\ \dot{\psi} \end{pmatrix} = \begin{bmatrix} 1 & s_\phi s_\theta/c_\theta & c_\phi s_\theta/c_\theta \\ 0 & c_\phi & -s_\phi \\ 0 & s_\phi/c_\theta & c_\phi/c_\theta \end{bmatrix} \begin{pmatrix} p \\ q \\ r \end{pmatrix}. \tag{49.9}$$

Note that the above equation has singularity at $\theta = 90°$. If full-envelope flight is required, a quaternion representation is recommended. However, normal maneuvering of a coaxial helicopter will not hit such an extreme condition. Thus, it is still adequate to use this relatively simple equation.

Next, by treating the whole coaxial platform as a rigid mass, the 6DoF dynamics can be described by the following Newton-Euler equations:

$$\begin{pmatrix} \dot{u} \\ \dot{v} \\ \dot{w} \end{pmatrix} = \frac{1}{m} \begin{pmatrix} F_x \\ F_y \\ F_z \end{pmatrix} - \begin{pmatrix} p \\ q \\ r \end{pmatrix} \times \begin{pmatrix} u \\ v \\ w \end{pmatrix}, \tag{49.10}$$

$$\begin{pmatrix} \dot{p} \\ \dot{q} \\ \dot{r} \end{pmatrix} = \mathbf{J}^{-1} \left\{ \begin{pmatrix} M_x \\ M_y \\ M_z \end{pmatrix} - \begin{pmatrix} p \\ q \\ r \end{pmatrix} \times \mathbf{J} \begin{pmatrix} p \\ q \\ r \end{pmatrix} \right\}, \tag{49.11}$$

where F_x, F_y, F_z are projections of the net force, $\mathbf{F}$, onto the helicopter body-frame x-, y-, z-axis and M_x, M_y, M_z are projections of the net torque, $\mathbf{M}$, onto the body-frame x-, y-, z-axis. The compositions of $\mathbf{F}$ and $\mathbf{M}$ come from

various parts of the coaxial helicopter. For the fixed-pitch and variable-pitch coaxial helicopters, although their force and torque compositions are more or less the same (explained in Sect. 49.3.3), the individual force and torque generation will have different formulations because of their different working principles (explained in Sects. 49.3.4 and 49.3.5, respectively). Till now, the unknown parameters that need to be identified are m, the total mass of the platform, and $\mathbf{J}$, the moment of inertia of the platform, which is in the form of

$$\mathbf{J} = \begin{bmatrix} J_{xx} & -J_{xy} & -J_{xz} \\ -J_{xy} & J_{yy} & -J_{yz} \\ -J_{xz} & -J_{yz} & J_{zz} \end{bmatrix}.$$

Since the coaxial helicopters are normally designed to be symmetric in both longitudinal and lateral directions, J_{xy}, J_{xz}, J_{yz} are extremely small and can be assumed to be zero. The identification method of J_{xx}, J_{yy}, J_{zz} will be explained in Sect. 49.4, which talks about various approaches in the problem of model-based parameter identification.

49.3.3 Force and Torque Composition

As mentioned in Sect. 49.3.2, forces and torques acting on the coaxial helicopter come from various mechanical parts. First of all, the helicopter weight exerts a force of mg in the NED-frame z-axis. After converting it to the body frame, the vector is shown as the second term on the right-hand side of Eq. 49.12.

Next, when the rotor blades spin, they generate thrusts, $\mathbf{T}_i$ ($i =$ up, dw), in the direction perpendicular to their respective tip path plane (TPP). When the upper and lower TPPs deviate from their default orientation, the thrust vectors no longer pass through the CG of the helicopter, thus creating rotational torque. The torque vectors caused by the rotor thrusts can be calculated by $\mathbf{l}_{up} \times \mathbf{T}_{up}$ and $\mathbf{l}_{dw} \times \mathbf{T}_{dw}$, where $\mathbf{l}_{up}$ and $\mathbf{l}_{dw}$ are the displacement vectors from helicopter CG to the upper rotor hub, and the lower rotor hub respectively. The deviation of the TPP can be described by the longitudinal flapping angle a_i and the lateral flapping angle b_i. The thrust decomposition to the body-frame axes can be approximated by Eq. 49.14. Nonzero a_i and b_i also directly result in flapping torque on the rotor hub. This torque can be simplified as the second term on the right-hand side of Eq. 49.13, where K_β is called the effective spring constant, and it has the same value for both the upper and lower rotors provided they are rotating at approximately the same speed.

Furthermore, the rotation of the rotors creates the drag torque, $\mathbf{Q}_{up}$ and $\mathbf{Q}_{dw}$, around the body-frame z-axis. When the coaxial helicopter hovers without yaw motion, the two torques have the same magnitude, thus canceling each other. Else, if the net drag torque is nonzero, yaw acceleration is generated. In addition, the change of rotational speeds of the rotors also generates the so-called reaction torques on the helicopter body (denoted by $\mathbf{Q}_{r,up}$ and $\mathbf{Q}_{r,dw}$). They are described in (Eq. 49.16),

where J_{up} and J_{dw} are the moment of inertia of the upper rotor (with stabilizer bar) and the lower rotor with respect to the rotor shaft. They can be calculated by measuring the mass and dimension of the rotor blades and stabilizer bar and assuming a regular geometric shape.

Lastly, when the helicopter moves in air, its fuselage experiences drag forces, X_{fus}, Y_{fus}, Z_{fus}, due to air resistance. This drag force is usually related to the linear speed and up-front surface area of the aerial vehicle.

Equations (49.12) and (49.13) have summarized all the forces and torques mentioned above, with (49.14)–(49.16) explaining how to evaluate the individual terms:

$$\begin{pmatrix} F_x \\ F_y \\ F_z \end{pmatrix} = \sum \mathbf{T}_i + mg \begin{pmatrix} -s_\theta \\ s_\phi c_\theta \\ c_\phi c_\theta \end{pmatrix} + \begin{pmatrix} X_{fus} \\ Y_{fus} \\ Z_{fus} \end{pmatrix}, \tag{49.12}$$

$$\begin{pmatrix} M_x \\ M_y \\ M_z \end{pmatrix} = \sum \mathbf{l}_i \times \mathbf{T}_i + \sum K_\beta \begin{pmatrix} b_i \\ a_i \\ 0 \end{pmatrix} + \sum \mathbf{Q}_{d,i} + \sum \mathbf{Q}_{r,i}, \tag{49.13}$$

$$\mathbf{l}_i = |\mathbf{l}_i| \begin{pmatrix} 0 \\ 0 \\ -1 \end{pmatrix}, \quad \mathbf{T}_i = |\mathbf{T}_i| \begin{pmatrix} -\sin a_i \\ \sin b_i \\ -\cos a_i \cos b_i \end{pmatrix}, \tag{49.14}$$

$$\mathbf{Q}_{d,up} = |\mathbf{Q}_{d,up}| \begin{pmatrix} 0 \\ 0 \\ 1 \end{pmatrix}, \quad \mathbf{Q}_{d,dw} = |\mathbf{Q}_{d,dw}| \begin{pmatrix} 0 \\ 0 \\ -1 \end{pmatrix}, \tag{49.15}$$

$$\mathbf{Q}_{r,up} = J_{up} \dot{\Omega}_{up} \begin{pmatrix} 0 \\ 0 \\ 1 \end{pmatrix}, \quad \mathbf{Q}_{r,dw} = J_{dw} \dot{\Omega}_{dw} \begin{pmatrix} 0 \\ 0 \\ -1 \end{pmatrix}. \tag{49.16}$$

49.3.4 Force and Torque Formulation of Fixed-Pitch Coaxial Helicopter

The generation of individual forces and torques on the fixed-pitch coaxial and the variable-pitch coaxial has quite different formulations. In this section, a full formulation of the fixed-pitch coaxial force and torque generation will be provided. That means, by tracing all the formulas listed in this section, the forces and torques exerted on the fixed-pitch coaxial helicopter can be exhaustively related to the four fundamental inputs in a rigorous way.

49.3.4.1 Thrust and Torque from Rotors

Here, the magnitude of the rotor thrust and drag torque, $|\mathbf{T}_i|$ and $|\mathbf{Q}_{\mathrm{d},i}|$, will first be investigated. According to the aerodynamic actuator disk theory (Bramwell et al. 2001), the magnitude of thrust generated by the rotors can be formulated as follows:

$$|\mathbf{T}_i| = \rho C_{T,i} A (\Omega_i R)^2, \tag{49.17}$$

where ρ is the density of air, $C_{T,i}$ is the lift coefficient, A is the rotor disk area, Ω_i is the rotational speed of the rotor, and R is the rotor blade length. Since this is a fixed-pitch coaxial helicopter, $C_{T,i}$, like the other parameters in (49.17), is constant. The only variable is Ω_i. Hence, the equation can be simplified to

$$|\mathbf{T}_i| = k_{T,i} \Omega_i^2, \tag{49.18}$$

where $k_{T,i}$ is a lumped thrust coefficient that needs to be identified. Similar assumptions and formulation can be applied to the relationship between the drag torque and the rotational speed of the rotors:

$$|\mathbf{Q}_{\mathrm{d},i}| = k_{Q,i} \Omega_i^2. \tag{49.19}$$

49.3.4.2 Rotor Flapping Dynamics

For this specific type of coaxial helicopter, the rotor collective pitch is fixed, while the cyclic pitch can be changed. For the lower rotor, the rotor hub is connected to the aileron and the elevator servos via a swashplate. When the swashplate tilts, it teeters the rotor hub and creates a cyclic pitch on the rotor. For every cycle of rotation, the rotor blade will reach the maximum angle of attack at a particular phase angle at which the lift on the blade is largest. This results in the flapping of the rotor disk. The whole mechanism is a combination of gyroscopic precession and aerodynamic precession. For the case of ESky Big Lama, if one observes the rotor blade in a slow motion, the maximum rotor flapping occurs roughly at 45° lag with respect to the occurrence of maximum angle of attack. This explains why the aileron and elevator servos of the off-the-shelf coaxial platform are connected to the swashplate 45° off the body-frame x-, y-axis. In this way, the aileron servo mainly controls the lateral flapping of the lower rotor, and the elevator servo mainly controls the longitudinal flapping. However, the flapping phase lag is not exactly equal to 45° (slightly larger than 45° from test bench observations) due to mechanical modifications to the original RC platform (original rotor blades have been replaced by stiffer ones for larger payload). This results in non-negligible coupling between the servo inputs and the lower rotor longitudinal and lateral flapping angles. As the lower rotor does not have any additional damping mechanism attached, its flapping process is almost instantaneous. By assuming a first-order dynamics, the time constant can be observed via a high-speed camera. The result turns out to be 0.0375 s (see Fig. 49.6), which is very small as compared to dynamics of other parts of the coaxial helicopter

Fig. 49.6 Step response of
servo motion attached to the
lower rotor (*top*: $t = 0$;
center, $t \approx 0.0375$ s; *bottom*,
$t = \infty$). This figure looks
dim because it was taken by a
high-speed camera

and thus can be ignored. Hence, the relationship between servo inputs and lower rotor flapping angles can be formulated in a static way:

$$a_{\text{dw}} = A_{a,\text{dw}}\, \delta_{\text{ele}} + A_{b,\text{dw}}\, \delta_{\text{ail}} - A_q\, q, \tag{49.20}$$

$$b_{\text{dw}} = B_{b,\text{dw}}\, \delta_{\text{ail}} + B_{a,\text{dw}}\, \delta_{\text{ele}} - B_p\, p, \tag{49.21}$$

where aileron (δ_{ail}) and elevator (δ_{ele}) are the servo inputs, $A_{a,\text{dw}}$ and $B_{b,\text{dw}}$ are the on-axis steady-state ratio from servo inputs to flapping angles, and $A_{b,\text{dw}}$ and $B_{a,\text{dw}}$ are the off-axis (coupling) values. The last term which depends on angular rates, p and q, comes from an effect called rotor damping, which was considered in literature either in linear or quadratic form. Here, a linear form is chosen because of its simplicity.

For the upper rotor system, a stabilizer bar is attached to the rotor hub, so that they teeter together. As the stabilizer bar has large moment of inertia, it tends to remain at its original rotating plane. Hence, at the moment when the helicopter body tilts, the stabilizer bar TPP will remain at the level plane, thus creating a cyclic pitch on the upper rotor which leads to blade flapping. The torque generated by this flapping redresses the rotational motion of the helicopter and significantly stabilizes the whole platform attitude. Similar to the lower rotor system, the stabilizer bar is installed at 45° phase lead to the rotor blade. In this way, the maximum flapping happens at the direction that precisely counters the rotational motion of the helicopter. Again, there is coupling between the longitudinal and lateral channels because the flapping phase lag is not exactly 45°. The following equations describe the above mentioned dynamics:

$$\dot{\phi}_{\text{sb}} = \frac{1}{\tau_{\text{sb}}}\, (\phi - \phi_{\text{sb}}), \tag{49.22}$$

$$\dot{\theta}_{\text{sb}} = \frac{1}{\tau_{\text{sb}}}\, (\theta - \theta_{\text{sb}}), \tag{49.23}$$

$$a_{\text{up}} = A_{a,\text{up}}\, (\theta_{\text{sb}} - \theta) + A_{b,\text{up}}\, (\phi_{\text{sb}} - \phi) - A_q\, q, \tag{49.24}$$

$$b_{\text{up}} = B_{b,\text{up}}\, (\phi_{\text{sb}} - \phi) + B_{a,\text{up}}\, (\theta_{\text{sb}} - \theta) - B_p\, p, \tag{49.25}$$

where ϕ_{sb} and θ_{sb} are the roll and pitch angles of the stabilizer bar TPP, $A_{a,\text{up}}$ and $B_{b,\text{up}}$ are the on-axis steady-state ratio from the stabilizer bar teetering angles to the upper rotor flapping angles, and $A_{b,\text{up}}$ and $B_{a,\text{up}}$ are the off-axis (coupling) values. τ_{sb} is the time constant of approximated first-order flapping dynamics. Again, the same rotor damping effects (terms depending on p and q) are considered for the upper rotor flapping dynamics.

49.3.4.3 Fuselage Drag

When the helicopter fuselage moves in air, it experiences drag force acting on the opposite direction of the motion. For the body-frame horizontal directions, the rotor

downwash is deflected by u and v. In the situation when u (or v) is less than v_i (the induced velocity of air at the lower rotor), the downwash effect needs to be taken into account. Otherwise, the downwash effect is relatively weak and can be ignored. The fuselage in all three directions is considered as a flat plate perpendicular to the helicopter motion; thus, the drag coefficient is approximately unity. As such, the horizontal fuselage drag forces are formulated in a quadratic form:

$$X_{\text{fus}} = -\frac{\rho}{2} S_x u \cdot \max(v_i, |u|), \tag{49.26}$$

$$Y_{\text{fus}} = -\frac{\rho}{2} S_y v \cdot \max(v_i, |v|), \tag{49.27}$$

$$v_i = \sqrt{\frac{|T_{\text{dw}}|}{2\rho\pi R^2}}, \tag{49.28}$$

where S_x and S_y are the effective drag area along the body-frame x- and y-axis, respectively.

For the vertical direction, since the fuselage is constantly exposed to the lower rotor downwash, it is commonly formulated in the following form:

$$Z_{\text{fus}} = -\frac{\rho}{2} S_z (w - v_i)|w - v_i|. \tag{49.29}$$

However, as the lift coefficient test for identifying $k_{T,i}$ in Eq. 49.18 was done with the presence of the fuselage (so the term $\frac{\rho}{2} S_z v_i^2$ has already been taken into account), the above equation needs to be compensated as

$$Z_{\text{fus}} = -\frac{\rho}{2} S_z w \cdot \max(v_i, |w|), \tag{49.30}$$

where S_z is the effective drag area along the body-frame z-axis.

49.3.4.4 Motor Speed Dynamics

Two brushless DC motors are used on the ESky Big Lama coaxial platform. Their rotational speed dynamics follows the well-known differential equation of electro motors:

$$J_{\text{mot}}\dot{\omega} = \frac{k_{\text{m}}U - k_{\text{m}}k_{\text{e}}\omega}{R_{\text{mot}}} - d\omega - M_{\text{L}}, \tag{49.31}$$

where J_{mot} is the motor moment of inertia, k_{m} and k_{e} are the mechanical and electrical motor constants, U is the input voltage, R_{mot} is the resistance of the circuit, d is the friction coefficient, and M_{L} is the external torque acting on the motor shaft. Here, M_{L} is equal to the rotor drag torque $Q_{\text{d},i}$ appeared in Eq. 49.19. If the helicopter operates at a near-hover condition, everything can be approximated as linear. M_{L} can be assumed to be a combination of a constant trimming value, M_{L}^*,

and another term proportional to extra rotational speed as compared to the trimming speed, Ω^*:

$$M_L = M_L^* + k_L(\Omega - \Omega^*). \tag{49.32}$$

By further considering that the rotational speed of rotor, Ω, and the rotational speed of the motor, ω, are perfectly proportional by the gear ratio, the rotor speed dynamics can be simplified to the following first-order equations:

$$\dot{\Omega}_{up} = \frac{1}{\tau_{mt}}(m_{up}\delta_{up} + \Omega_{up}^* - \Omega_{up}), \tag{49.33}$$

$$\dot{\Omega}_{dw} = \frac{1}{\tau_{mt}}(m_{dw}\delta_{dw} + \Omega_{dw}^* - \Omega_{dw}), \tag{49.34}$$

where Ω_{up}^* and Ω_{dw}^* are the trimming values of the rotor rotational speed at hovering, τ_{mt} is the time constant of the motor speed dynamics, and m_{up}, m_{dw} are the steady-state ratio between the change of rotor speeds and the change of motor inputs.

49.3.4.5 Mixer and Headlock Gyro Dynamics
In order to largely decouple the throttle-heave and the rudder-yaw dynamics, the throttle and rudder signals are passed into a hardware mixer and transformed to dual motor control signals:

$$\delta_{up} = \delta_{thr} + \bar{\delta}_{rud}, \tag{49.35}$$

$$\delta_{dw} = \delta_{thr} - \bar{\delta}_{rud}. \tag{49.36}$$

It can be seen that when the throttle signal δ_{thr} increases, inputs to both motors increase; when the rudder signal $\bar{\delta}_{rud}$ increases, the input to the motor connected to the upper rotor increases while the input to the motor connected to the lower rotor decreases.

Note that the rudder signal in the above mixer equation is not the original signal δ_{rud}. From δ_{rud} to $\bar{\delta}_{rud}$, there is a hardware headlock gyro which helps refine the rudder signal and acts as the most inner-loop yaw motion stabilizer. Usually, there is a PI controller embedded inside the headlock gyro, and it can be formulated as follows:

$$\dot{r}_{fb} = K_a\delta_{rud} - r, \tag{49.37}$$

$$\bar{\delta}_{rud} = K_P(K_a\delta_{rud} - r) + K_I r_{fb}, \tag{49.38}$$

where r_{fb} is the augmented state variable needed by the integral control. At this point, the full dynamics of a coaxial helicopter have been mathematically formulated, but the model parameters are yet to be identified. In Sect. 49.4, the identification methods will be comprehensively given.

49.3.5 Force and Torque Formulation of Variable-Pitch Coaxial Helicopter

For the case of the variable-pitch coaxial helicopter, the formulation of force and torque generation will not be thoroughly listed as some of the formulas are very much like its fixed-pitch counterpart. For example, the formulas about fuselage drag and the headlock gyro PI controller are more or less the same. As such, only formulations that have significant differences when compared to the fixed-pitch coaxial case will be listed and explained here.

It should also be noted that the main differences compared occur in two areas, namely, the rotor thrust generation and the rotor flapping dynamics. In this section, the formulations about thrust generation and rotor flapping dynamics of the variable-pitch coaxial helicopter will be derived from a more fundamental perspective, thus capturing more aerodynamic details. This also reflects the fact that model formulation of aerial vehicles can be done at different levels of complexity. If the model is to be used for accurate structural analysis and optimization or controller design for aggressive maneuvering, then a more precise and complicated modeling approach should be adopted. However, if the planned flight missions are relatively stable and peaceful, a simplified model formulation is usually more than enough, such as that of the fixed-pitch coaxial case.

Thorough aerodynamics study of coaxial rotor system is itself a big research topic. NASA researcher (Colin 1997) has provided a good survey covering the aerodynamics research worldwide, including America, Russia, Japan, and Germany. Of all the surveyed techniques, blade element momentum theory (BEMT) (Leishman 2006) is a standard method for preliminary rotor analysis before complex high-level analysis, such as free vortex models (FVM) and Lagrangian particle vortex methods (LPVM). In this chapter, the detailed derivation and reasoning of BEMT will not be repeated. Only the main computation procedures are listed for easier reference and understanding.

49.3.5.1 Thrust and Torque from Rotors

The formal analysis of helicopter rotor motion usually starts from its thrust, torque, and power generation. The rotor thrust, torque, and power can be expressed as

$$T = \rho C_T A \Omega^2 R^2, \tag{49.39}$$

$$Q = \rho C_Q A \Omega^2 R^3, \tag{49.40}$$

$$P = \rho C_P A \Omega^3 R^3. \tag{49.41}$$

Here, ρ is the air density, A is the rotor disk area, Ω is the rotor rotational speed, and R is the rotor radius. C_T, C_P, C_Q are the rotor thrust coefficient, power coefficient, and torque coefficient, respectively. It should be noted that the power is related to torque by $P = \Omega Q$. Hence, $C_P = C_Q$ numerically. All the parameters in Eqs. 49.39–49.41 are constant except for the three coefficients C_T, C_P, C_Q.

First of all, the incremental thrust coefficient is defined as

$$\mathrm{d}C_T = \frac{1}{2}\sigma C_l r^2 \mathrm{d}r = \frac{\sigma C_{l_\alpha}}{2}(\theta_u r^2 - \lambda r)\mathrm{d}r, \qquad (49.42)$$

where C_{l_α} is the lift-curve slope of the airfoil section, which can be obtained by checking the official wind tunnel test results if the blade airfoil is standard. σ is the rotor solidity defined as the ratio of the blade area against the rotor disk area. θ_u is the blade pitch distribution on the upper rotor. r is the nondimensional radial distance along the blade. λ is the nondimensional induced velocity which can be expressed in terms of r and λ_∞ as

$$\lambda(r, \lambda_\infty) = \sqrt{\left(\frac{\sigma C_{l_\alpha}}{16F} - \frac{\lambda_\infty}{2}\right)^2 + \frac{\sigma C_{l_\alpha}}{8F}\theta_u r} - \left(\frac{\sigma C_{l_\alpha}}{16F} - \frac{\lambda_\infty}{2}\right), \qquad (49.43)$$

where F is the factor to account for the Prandtl tip loss defined as

$$F = \left(\frac{2}{\pi}\right) \cos^{-1}(e^{-f}), \qquad (49.44)$$

where f is given in terms of the number of blades N_b and the radial position of the blade element r:

$$f = \frac{N_b}{2}\left(\frac{1-r}{r\phi}\right), \qquad (49.45)$$

and ϕ is the induced inflow angle, which equals to $\lambda(r)/r$.

For both the upper and lower rotors, the same principles can be applied. However, as the inner part of the lower rotor operates in the *vena contracta* of the upper rotor, the analysis can be more complicated. From the flow visualization results of Taylor (1950), the author stated that the wake of the upper rotor contracts fully within $0.25R$ below the upper rotor. The ideal wake contraction ratio, r_c, is 0.707, but in practice it is found closer to 0.8. The contracted wake is defined as $A_c = \pi r_c^2 R^2$. The inner area of the lower rotor encounters incoming stream-tubes with velocity $V_\infty + (A/A_c)v_u$ ($V_\infty + 2v_u$ in the ideal case). For beam sections lying inside the upper rotor contraction area, the inflow distribution is given as

$$\lambda(r, \lambda_\infty) = \sqrt{\left(\frac{\sigma C_{l_\alpha}}{16F} - \frac{\lambda_\infty + (A/A_c)\lambda_u}{2}\right)^2 + \frac{\sigma C_{l_\alpha}}{8F}\theta_l r}$$
$$- \left(\frac{\sigma C_{l_\alpha}}{16F} - \frac{\lambda_\infty + (A/A_c)\lambda_u}{2}\right), \qquad (49.46)$$

where θ_l is the blade pitch distribution on the lower rotor. For points outside the contraction area, the inflow distribution is given as

$$\lambda(r, \lambda_\infty) = \sqrt{\left(\frac{\sigma C_{l_\alpha}}{16F} - \frac{\lambda_\infty}{2}\right)^2 + \frac{\sigma C_{l_\alpha}}{8F}\theta_l r} - \left(\frac{\sigma C_{l_\alpha}}{16F} - \frac{\lambda_\infty}{2}\right). \qquad (49.47)$$

When the inflow velocity distribution is obtained, the total thrust lift coefficient could be found by integrating Eq. 49.42 as

$$C_T = \int_{r=0}^{r=1} \mathrm{d}C_T. \qquad (49.48)$$

For the rotor torque coefficient and power coefficient, their incremental calculation is also provided by BEMT:

$$\mathrm{d}C_Q = \mathrm{d}C_P = \frac{\sigma}{2}(\phi C_l + C_\mathrm{d})r^3\mathrm{d}r, \qquad (49.49)$$

where C_d is the rotor drag coefficient. By knowing the fact that $\lambda = \phi r$, the incremental power is defined as

$$\begin{aligned}
\mathrm{d}C_P &= \frac{\sigma}{2}\phi C_l r^3\mathrm{d}r + \frac{\sigma}{2}C_\mathrm{d}r^3\mathrm{d}r \\
&= \frac{\sigma}{2}C_l\lambda r^2\mathrm{d}r + \frac{\sigma}{2}C_\mathrm{d}r^3\mathrm{d}r \\
&= \mathrm{d}C_{P_u} + \mathrm{d}C_{P_o}.
\end{aligned} \qquad (49.50)$$

The induced power coefficient can be obtained by integrating $\mathrm{d}C_{P_u}$ as follows:

$$C_{P_u} = \int_{r=0}^{r=1} \mathrm{d}C_{P_u} = \int_{r=0}^{r=1} \lambda\,\mathrm{d}C_{T_u}, \qquad (49.51)$$

and the profile part of the rotor power is given by

$$C_{P_o} = \frac{\sigma}{2}\int_0^1 C_\mathrm{d}r^3\mathrm{d}r. \qquad (49.52)$$

49.3.5.2 Bare Rotor Flapping Dynamics

Similar to that of the fixed-pitch coaxial case, the rotor flapping dynamics of the variable-pitch coaxial helicopter is also seen as a rigid disk which can tilt about its longitudinal and lateral axes. However, instead of directly linking the flapping angles' dynamics to the servo inputs, the flapping angles (a_i, b_i) are first related to the cyclic pitch angles $(\theta_{\mathrm{cyc},bi}, \theta_{\mathrm{cyc},ai})$ as intermediate variables. The presence of $\theta_{\mathrm{cyc},bi}$ and $\theta_{\mathrm{cyc},ai}$ is a joint consequence of servo inputs and the stabilizer bar flapping angles. The detailed description of the rotor equations is extremely complicated. Here, a simplified formulation is adopted, where the rotor forces and moments are expressed as a polynomial function of the rotor state variables (Mettler 2002).

By removing the higher-order terms of the TPP equation, the remaining first-order rotor dynamics could be expressed as

$$\tau \dot{b}_i = -b_i - \tau p + B_a a_i + \theta_{\text{cyc}, bi}, \tag{49.53}$$

$$\tau \dot{a}_i = -a_i - \tau q + A_b b_i + \theta_{\text{cyc}, ai}, \tag{49.54}$$

where

$$A_b = -B_a = \frac{8 K_\beta}{\gamma \Omega^2 J_\beta}, \tag{49.55}$$

$$\tau = \frac{16}{\gamma_r \Omega} \left(1 - \frac{8e}{3R} \right)^{-1}, \tag{49.56}$$

$$\gamma = \frac{\rho c C_{l\alpha} R^4}{J_\beta}. \tag{49.57}$$

a_i and b_i are the first-order TPP flapping angles in the longitudinal and lateral directions for either the upper rotors or the lower rotors. τ and γ are the flapping time constant and the lock number of the rotor blades, respectively. J_β is the blade moment of inertia. $\theta_{\text{cyc}, ai}$ and $\theta_{\text{cyc}, bi}$ are the longitudinal and lateral cyclic pitch of rotor blade. The other terms are defined by the same symbols as that of the fixed-pitch coaxial helicopter analysis in Sect. 49.3.4. The approximate formulation in Eqs. 49.53 and 49.54 characterizes the crucial TPP responses with respect to rotor cyclic control inputs.

49.3.5.3 Stabilizer Bar Flapping Dynamics

The stabilizer bar, which is attached to the upper main rotor shaft via a free-teetering hinge, can be regarded as a third disk. It consists of two paddles and a steel rod. The stabilizer bar is not designed to produce thrust or moment on the main hub, whereas its main function is to adjust the helicopter dynamics via the Bell-Hiller mixer by augmenting the cyclic pitch command of the upper rotor. It serves as a feedback system which increases the helicopter robustness against wind gust and turbulence (Cai et al. 2011). The flapping dynamics of stabilizer bar can be expressed as two first-order differential equations:

$$\dot{\phi}_{\text{sb}} = -q - \frac{1}{\tau_{\text{sb}}} \phi_{\text{sb}} + \frac{C}{\tau_{\text{sb}}} \delta_{\text{ail}}, \tag{49.58}$$

$$\dot{\theta}_{\text{sb}} = -p - \frac{1}{\tau_{\text{sb}}} \theta_{\text{sb}} + \frac{D}{\tau_{\text{sb}}} \delta_{\text{ele}}, \tag{49.59}$$

where τ_{sb} is the stabilizer bar flapping time constant, and it can be calculated as

$$\tau_{\text{sb}} = \frac{16}{\gamma_{\text{sb}} \Omega}, \tag{49.60}$$

where γ_{sb} is the stabilizer bar lock number:

$$\gamma_{sb} = \frac{\rho c_{sb} C_{l\alpha,sb} \left(R_{sb}^4 - r_{sb}^4\right)}{I_{\beta,sb}}. \tag{49.61}$$

The free-teetering hinge does not constrain the flapping of the stabilizer bar; thus, there is no coupling between the longitudinal and lateral flapping motions. The augmented rotor cyclic pitch of upper rotor can be expressed as

$$\theta_{cyc,aup} = A_a \delta_{ele} + K_{sb}\phi_{sb}, \tag{49.62}$$

$$\theta_{cyc,bup} = B_b \delta_{ail} + K_{sb}\theta_{sb}, \tag{49.63}$$

where K_{sb} is the ratio of rotor blade cyclic pitch to stabilizer bar flapping.

49.3.5.4 Lumped Flapping Dynamics

In this variable-pitch coaxial configuration, the upper rotor and the lower rotor receive the same cyclic input (δ_{ail}, δ_{ele}) since the top swashplate and bottom swashplate are always parallel. To minimize the overall complexity of the model, the two counterrotating rotor disks are treated as one equivalent rotor disk with respect to flapping motions. This assumption is only valid when the helicopter does not perform rapid maneuvering. By making this assumption, the model can be simplified to a large extent yet maintaining reasonable fidelity. The imaginary rotor has equivalent longitudinal and lateral angles expressed as a_s and b_s. Combining Eqs. 49.53–49.63, the lumped flapping dynamics subsystem could be represented in the following state-space form:

$$\dot{\mathbf{x}} = \mathbf{A}\,\mathbf{x} + \mathbf{B}\,\mathbf{u}, \tag{49.64}$$

$$\dot{\mathbf{y}} = \mathbf{C}\,\mathbf{x}, \tag{49.65}$$

where

$$\mathbf{x} = \begin{pmatrix} p \\ q \\ a_s \\ b_s \end{pmatrix}, \quad \mathbf{u} = \begin{pmatrix} \delta_{ail} \\ \delta_{ele} \end{pmatrix}, \quad \mathbf{y} = \begin{pmatrix} p \\ q \end{pmatrix}, \tag{49.66}$$

$$\mathbf{A} = \begin{bmatrix} 0 & 0 & 0 & L_b \\ 0 & 0 & M_a & 0 \\ 0 & -1 & -\dfrac{1}{\tau_s} & \dfrac{A_b}{\tau_s} \\ -1 & 0 & \dfrac{B_a}{\tau_s} & -\dfrac{1}{\tau_s} \end{bmatrix}, \quad \mathbf{B} = \begin{bmatrix} 0 & 0 \\ 0 & 0 \\ 0 & A'_{lon} \\ B'_{lat} & 0 \end{bmatrix}, \quad \mathbf{C} = \begin{bmatrix} 1 & 0 & 0 & 0 \\ 0 & 1 & 0 & 0 \end{bmatrix}, \tag{49.67}$$

$$L_b = \frac{mg\,H_{mr} + K_\beta}{J_{xx}}, \quad M_a = \frac{mg\,H_{mr} + K_\beta}{J_{yy}}. \tag{49.68}$$

49.4   Model-Based Parameter Identification

When model formulation of a certain type of aerial platform has been derived, the next step is to identify unknown parameters of the derived model for a particular case. This is commonly known as the model-based parameter identification. In this section, several common parameter identification methods will be introduced based on the case study of ESky Big Lama, belonging to the fixed-pitch coaxial helicopter. It will be seen that some of the model parameters can be directly measured, while the remaining ones need special test bench experiments or flight tests to be carried out. The identification procedures for the case of variable-pitch coaxial helicopter will not be repeated since similar methods can be applied. It is also hoped that the readers will try the suggested experimental setups on other types of aerial platforms if they face similar parameter identification problems in their UAV-related projects.

49.4.1 Direct Measurement

For the ESky Big Lama fixed-pitch coaxial helicopter, some of its model parameters, especially those inherently defined by the platform dimension, geometry, weight loading, and the operational environment, can be directly measured or algebraically calculated, for example, the total mass of the platform (m), the distance from the rotor hubs to CG ($|\mathbf{l}_{\mathrm{up}}|$ and $|\mathbf{l}_{\mathrm{dw}}|$), the air density ($\rho$), the rotor diameter ($R$), the effective drag area of the fuselage (S_x, S_y, S_z), and the moment of inertia of the upper and lower rotor system (J_{up}, J_{dw}). Table 49.4 shows all the parameter values that can be identified through direct measurement and simple calculation.

49.4.2 Test Bench Experiment

In most aerial vehicle modeling cases, the direct measurement method is only able to determine a small portion of the parameters. The remaining majority parameters have to be identified by additional test bench experiments or actual flight tests. In this subsection, some common test bench methods are introduced, and they are again illustrated based on the ESky Big Lama fixed-pitch coaxial helicopter case.

First of all, the diagonal elements of the helicopter moment of inertia matrix J_{xx}, J_{yy}, J_{zz} can be measured by the so-called trifilar pendulum method proposed in Harris (1996). The experimental setup is shown in Fig. 49.7. In this experiment, the coaxial platform is suspended by three flexible strings with equal length l. The horizontal distances between the attached points and the CG are l_1, l_2, and l_3, respectively. One can slightly twist and release the platform around the z-axis and record the oscillation period t_l. The moment of inertia is then given by

$$J_{zz} = \frac{mgl_1l_2l_3t_l^2}{4\pi^2 l} \cdot \frac{l_1 \sin\alpha_1 + l_2 \sin\alpha_2 + l_3 \sin\alpha_3}{l_2l_3 \sin\alpha_1 + l_1l_3 \sin\alpha_2 + l_1l_2 \sin\alpha_3}, \tag{49.69}$$

**Table 49.4** Parameters determined via direct measurement

Parameter	Physical meaning
$\rho = 1.204$ kg m^{-3}	Air density
$m = 0.977$ kg	Total mass of the platform
$R = 0.250$ m	Rotor radius
$g = 9.781$ m s^{-2}	Earth gravity
$S_{fx} = 0.00835$ m^2	Effective longitudinal fuselage drag area
$S_{fy} = 0.01310$ m^2	Effective lateral fuselage drag area
$S_{fz} = 0.01700$ m^2	Effective vertical fuselage drag area
$|l_{\mathrm{up}}| = 0.195$ m	Distance from platform CG to the upper rotor hub
$|l_{\mathrm{dw}}| = 0.120$ m	Distance from platform CG to the lower rotor hub
$J_{\mathrm{up}} = 6.8613 \cdot 10^{-4}$ kg m^2	Moment of inertia of the upper rotor with stabilizer bar
$J_{\mathrm{dw}} = 3.2906 \cdot 10^{-4}$ kg m^2	Moment of inertia of the lower rotor
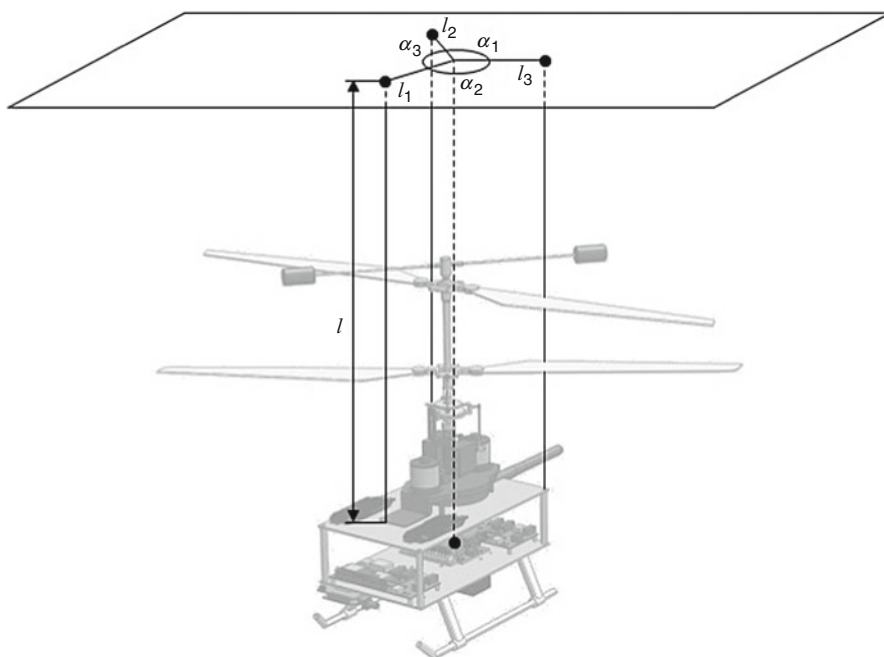
Fig. 49.7 The trifilar pendulum method

where α_1, α_2, and α_3 are the angles denoted in Fig. 49.7. Similar experiments can be done to obtain the moment of inertia around the y and z axes. Figure 49.8 shows the experimental setups to carry out this trifilar pendulum method to obtain the moment of inertia of the ESky Big Lama in all three axes.

Next, to identify the rotor thrust coefficient and torque coefficient ($k_{T,i}$ and $k_{Q,i}$), two self-designed test bench experiments were carried out
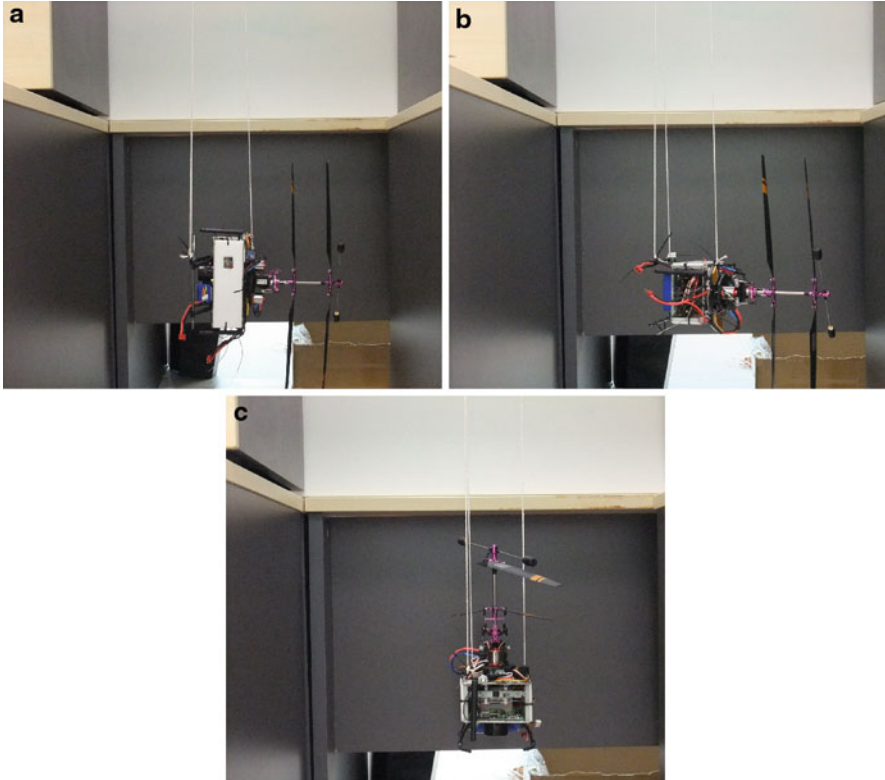
Fig. 49.8 The setups to test helicopter moment of inertia. (**a**) x-axis. (**b**) y-axis. (**c**) z-axis

(see Figs. 49.9 and 49.10). The main measurement sensors include a force meter and a tachometer. When different values of pulse width modulation (PWM) signals are given to the motors, the steady-state rotor rotational speed and the generated thrust/toque are recorded. For the thrust experiment, results are summarized in Fig. 49.11. There are four lines in the plot, in which two of them (solid lines) perfectly match. They represent the cases when only one rotor, either the upper rotor or the lower rotor, is rotating. The dashed line on the top is a numerical combination of the two solid lines, while the dash-dot line comes from the actual test with both rotors spinning at the same speed. The gap between the two lines shows a drop in thrust efficiency caused by aerodynamic interactions between the two rotors. According to Deng et al. (2003), for a coaxial helicopter operating in near-hover condition, the induced-velocity effect of the upper rotor to the lower rotor is significantly larger than that of the lower rotor to the upper rotor. Thus, the loss of thrust efficiency can be assumed to be fully absorbed by the lower rotor thrust coefficient. Hence, $k_{T,\mathrm{up}}$ is the gradient of the solid line, and $k_{T,\mathrm{dw}}$ is the gradient difference between the dash-dot line and the solid line. For the torque experiment, results are summarized in Fig. 49.12. The solid line represents the case when only

Fig. 49.9 Setup to investigate relation between rotor thrust and rotor rotational speed

Fig. 49.10 Setup to investigate relation between rotor torque and rotor rotational speed
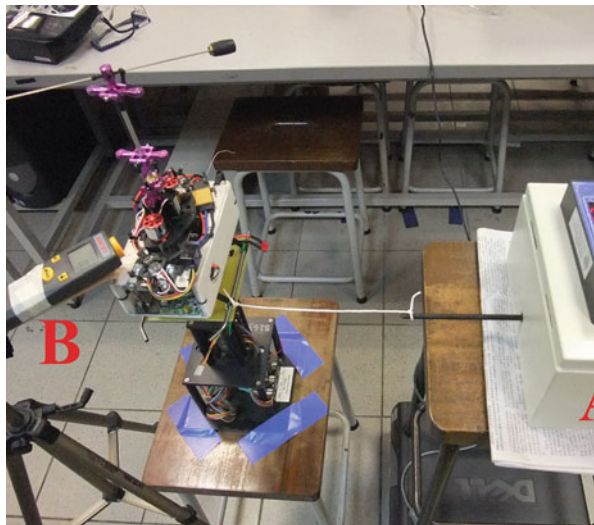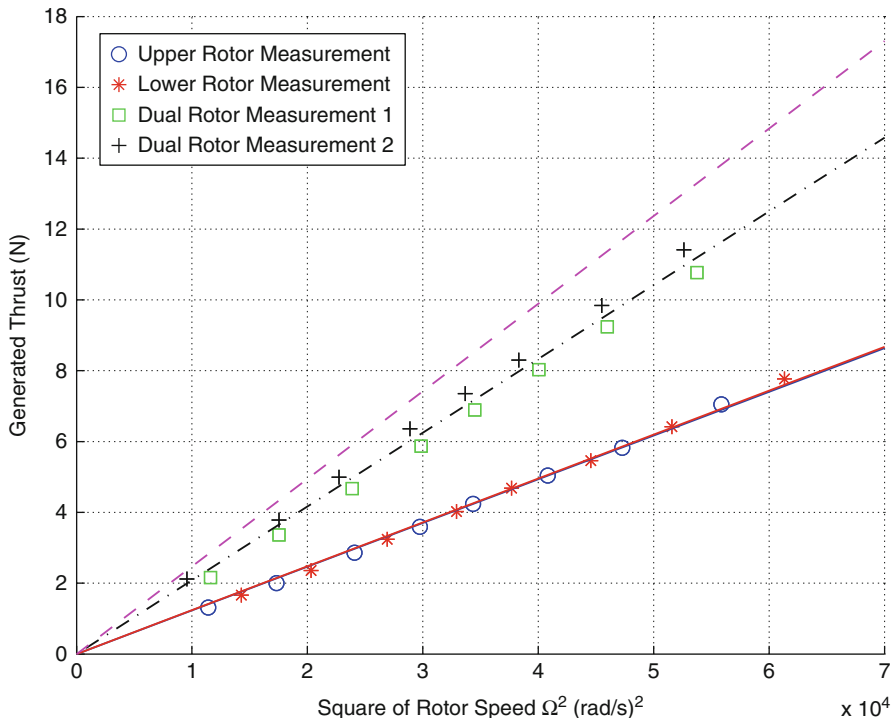
Fig. 49.11 Data plot of thrust against square of rotor speed

the stabilizer bar is rotating, while the dash-dot line is for a single rotating rotor. The dashed line is generated with the upper rotor and the stabilizer bar spinning together. Unsurprisingly, it matches the numerical combination of the lower two lines. Thus, the gradient of the dashed line is $k_{Q,\text{up}}$, and the gradient of the dash-dot line is $k_{Q,\text{dw}}$.

The identification of parameters involved in the motor dynamics can be done via test bench experiments also. The method to determine motor time constant (τ_{mt}) is a bit tricky, as the transient response of the rotor speed with a step motor input is very difficult to be recorded in real time. As such, instead of examining the transient response of the rotor speed with motor step input, the transient response of the input voltage subject to the changes of the motor Back-EMF (voltage generated by the spinning motor) is recorded using an oscilloscope (see Fig. 49.13). In theory, the time constant of the two transient responses should be the same. On the other hand, m_{up} and m_{dw} can be identified by plotting the steady-state relationship between the rotor speed and the normalized motor input (see Fig. 49.14). m_{up} and m_{dw} are the gradients of the two fitted lines in the figure.

The headlock gyro forms the most inner-loop control in the helicopter yaw channel. As mentioned in Sect. 49.3.4, it is a PI controller with three parameters (K_{a}, K_{P}, K_{I}) to be identified. The identification of K_{a} can be done via a hovering
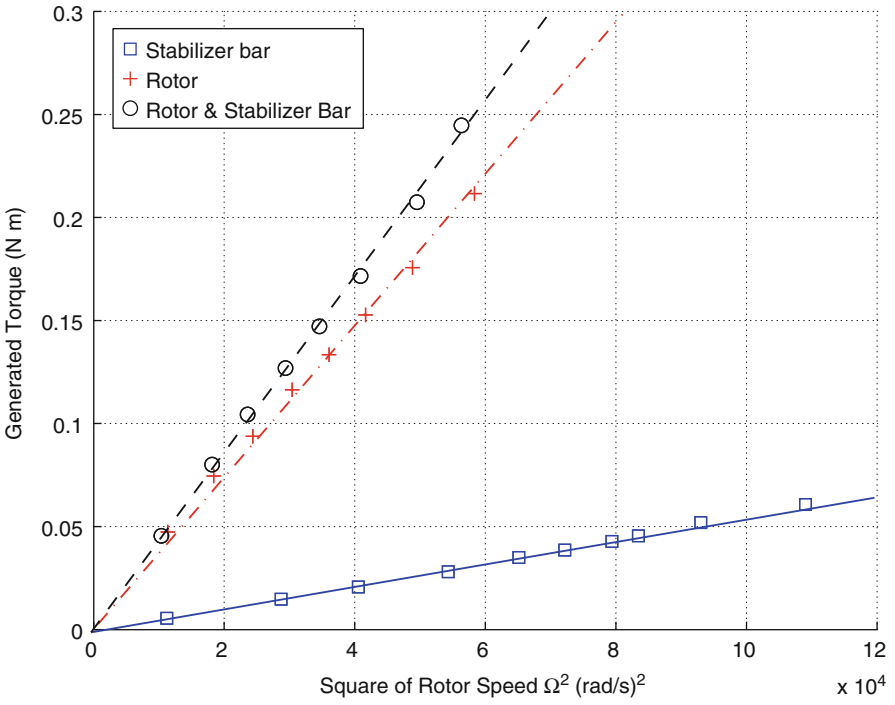
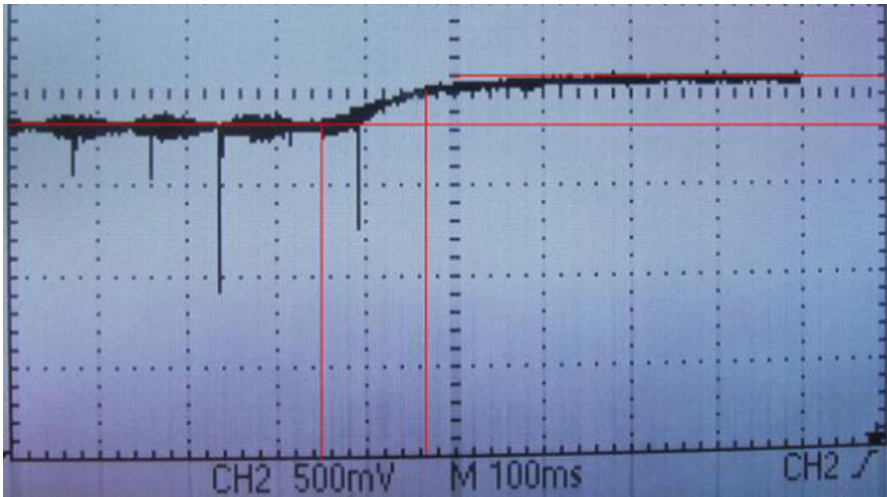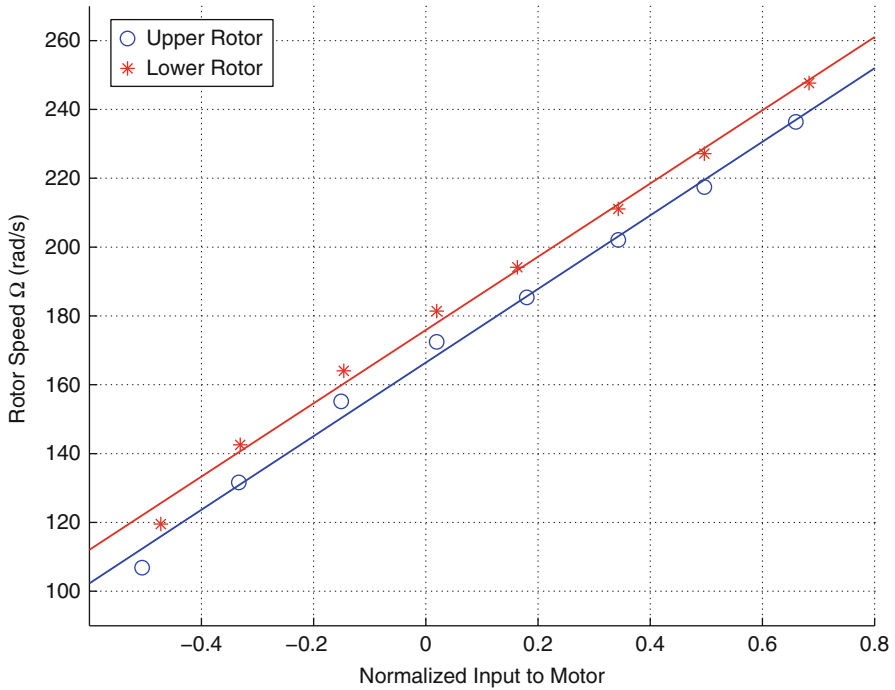**Fig. 49.12** Data plot of torque against square of rotor speed

**Fig. 49.13** Estimation of time constant of motor speed dynamics

Fig. 49.14 Data plot of rotor speed against motor input

Table 49.5 Yaw rate against rudder input

r (rad/s)	−1.50	−2.50	−2.60	−3.50
δ_{rud} (−1, 1)	0.25	0.35	0.40	0.55

turn test of the coaxial helicopter with different steady-state yaw rates. This test belongs more to the test bench category instead of flight test because it can be done on a swivel table with minimal friction. Table 49.5 shows four sets of data recorded. By plotting the least-square-fit line (see Fig. 49.15) and calculating its gradient, K_a can be determined. For the identification of K_P and K_I, the helicopter is placed stationary on a table. K_P and K_I can be determined by observing the headlock gyro output signal (in pulse width modulation form) caused by a small known step inputs. The initial ratio between the output and the input is $K_P \cdot K_a$, while the climbing rate of the step response is $K_I \cdot K_a$.

Last but not least, test bench experiments are also capable of determining some of the model parameters involved in the rotor flapping dynamics. First of all, by tilting the helicopter suddenly with rotor rotating at hovering speed and observing the transient step response of the stabilizer bar TPP (see Fig. 49.16) by a high-speed camera, the time constant (τ_{sb}) can be found to be about 0.2 s. In addition, the on-axis parameters that appear in the rotor flapping equations ($A_{a,up}$, $B_{b,up}$, $A_{a,dw}$, and $B_{b,dw}$) can be roughly identified by measuring lengths and angles under
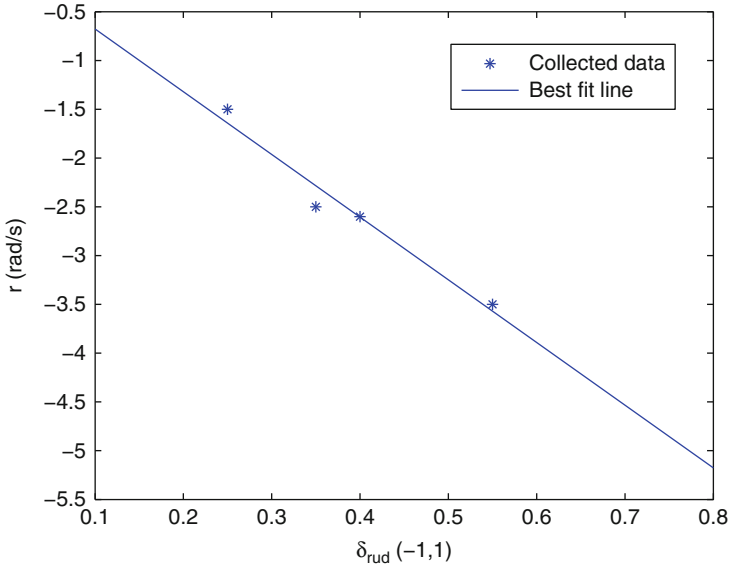
**Fig. 49.15** Data plot of yaw rate against rudder input

extreme conditions (see Figs. 49.17 and 49.18) and assume a linear proportional relationship between each pair of them. It should be noted that the parameters related to rotor flapping dynamics are most critical to the whole coaxial helicopter model. The above rough measurements may not be good enough to finalized their values. However, they can be used as an initial guess and get fine-tuned later by a model-based numerical search method via in-flight test data. In the next subsection, this method will be explained in detail. Here, Table 49.6 only lists those parameters that are already finalized at this test bench experiment stage.

49.4.3 Flight Test

After the majority of parameters have been identified, the remaining ones and a few uncertain ones can be identified and refined by analyzing flight test data with input perturbations (frequency sweeping). The recommended software for this task is called "Comprehensive Identification from FrEquency Responses" (CIFER). It is a MATLAB-based software package developed by NASA Ames Research Center for military-based rotorcraft system identifications.

In this ESky Big Lama case, since the remaining unidentified parameters are all about rotor flapping dynamics, only aileron and elevator perturbations need to be done to collect the relevant data for CIFER analysis. However, CIFER and most other parameter identification tools can only handle linear models. Hence, linearization needs to be done first to relate the aileron and elevator inputs to

Fig. 49.16 Step response of stabilizer bar TPP motion (*top*: $t = 0$; *center*, $t \approx 0.2\,\text{s}$; *bottom*, $t = \infty$)
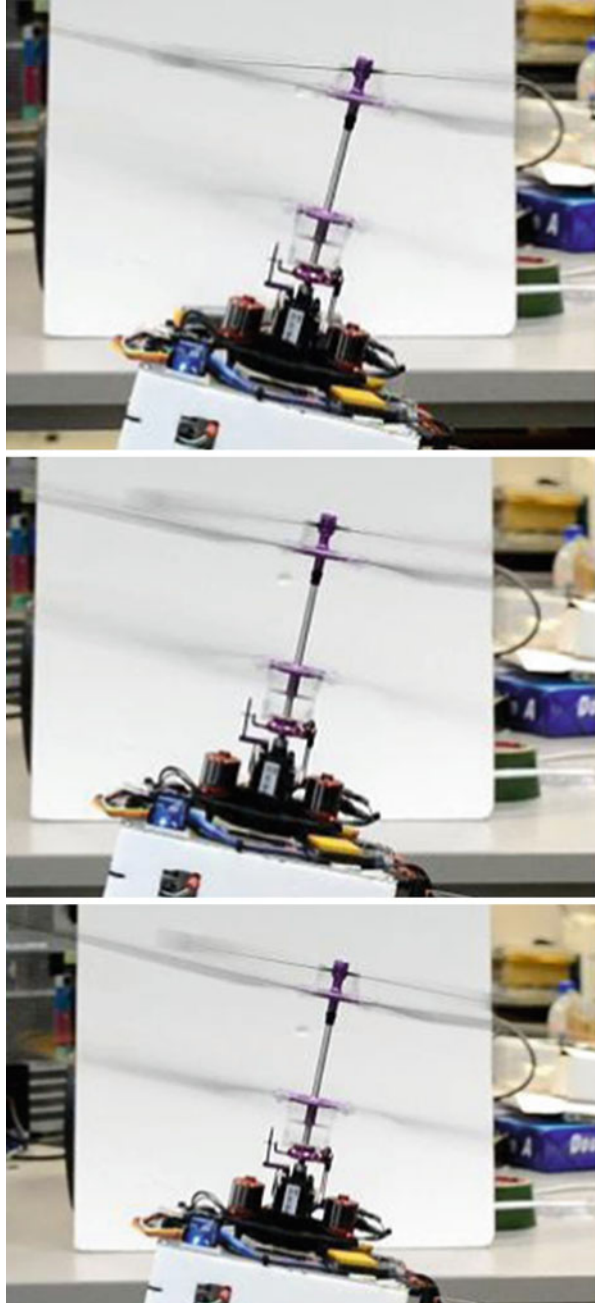
Fig. 49.17 *Left*: maximum teetering angle of the lower rotor hub; *right*: maximum flapping angle of the lower rotor
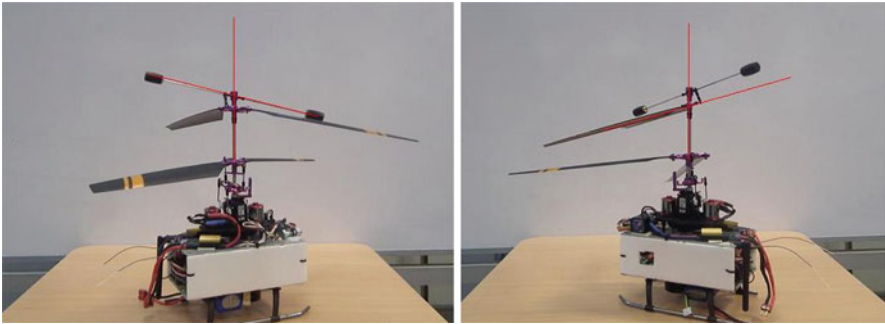
Fig. 49.18 *Left*: maximum teetering angle of the stabilizer bar; *right*: maximum teetering angle of the upper rotor hub

the helicopter roll, pitch angular rates. By relating and linearizing all the model formulation related to roll-pitch rate dynamics and upper rotor flapping dynamics at the hovering condition, one can obtain the following fourth-order linear state-space approximation:

$$
\begin{pmatrix} \dot{p} \\ q \\ a_{\text{up}} \\ b_{\text{up}} \end{pmatrix} =
\begin{bmatrix}
\frac{-X_{\text{dw}}B_{p,\text{dw}}}{J_{xx}} & 0 & 0 & \frac{X_{\text{up}}}{J_{xx}} \\
0 & \frac{-X_{\text{dw}}A_{q,\text{dw}}}{J_{yy}} & \frac{X_{\text{up}}}{J_{yy}} & 0 \\
-A_{b,\text{up}} & -A_{a,\text{up}} & -\frac{1}{\tau_{\text{sb}}} & 0 \\
-B_{b,\text{up}} & -B_{a,\text{up}} & 0 & -\frac{1}{\tau_{\text{sb}}}
\end{bmatrix}
\begin{pmatrix} p \\ q \\ a_{\text{up}} \\ b_{\text{up}} \end{pmatrix} +
\begin{bmatrix}
\frac{X_{\text{dw}}B_{b,\text{dw}}}{J_{xx}} & \frac{X_{\text{dw}}B_{a,\text{dw}}}{J_{xx}} \\
\frac{X_{\text{dw}}A_{b,\text{dw}}}{J_{yy}} & \frac{X_{\text{dw}}A_{a,\text{dw}}}{J_{yy}} \\
0 & 0 \\
0 & 0
\end{bmatrix}
\begin{pmatrix} \delta_{\text{ail}} \\ \delta_{\text{ele}} \end{pmatrix},
$$

$$(49.70)$$

where $X_{\text{up}} = T_{\text{up}}l_{\text{up}} + K_{\beta}$ and $X_{\text{dw}} = T_{\text{dw}}l_{\text{dw}} + K_{\beta}$. By treating $\delta_{\text{ail}}, \delta_{\text{ele}}$ as the inputs and p, q as the outputs (all can be recorded during flight tests) and giving known

Table 49.6 Parameters determined via test bench experiments

| Parameter	Physical meaning
$J_{xx} = 0.0059 \text{ kg m}^2$	Platform moment of inertia in the x-axis
$J_{yy} = 0.0187 \text{ kg m}^2$	Platform moment of inertia in the y-axis
$J_{zz} = 0.0030 \text{ kg m}^2$	Platform moment of inertia in the z-axis
$k_{T,\text{up}} = 1.23 \cdot 10^{-4} \text{ N s}^2\text{rad}^{-2}$	Effective thrust coefficient of the upper rotor
$k_{T,\text{dw}} = 8.50 \cdot 10^{-5} \text{ N s}^2 \text{ rad}^{-2}$	Effective thrust coefficient of the lower rotor
$k_{Q,\text{up}} = 4.23 \cdot 10^{-6} \text{ N ms}^2 \text{ rad}^{-2}$	Effective torque coefficient of the upper rotor
$k_{Q,\text{dw}} = 3.68 \cdot 10^{-6} \text{ N ms}^2 \text{ rad}^{-2}$	Effective torque coefficient of the lower rotor
$m_{\text{up}} = 106.90 \text{ rad s}^{-1}$	Steady-state ratio between change of upper rotor speed and change of motor input
$m_{\text{dw}} = 106.45 \text{ rad s}^{-1}$	Steady-state ratio between change of lower rotor speed and change of motor input
$\Omega^*_{\text{up}} = 203.38 \text{ rad s}^{-1}$	Trimming rotational speed of the upper rotor
$\Omega^*_{\text{dw}} = 217.88 \text{ rad s}^{-1}$	Trimming rotational speed of the lower rotor
$\tau_{\text{mt}} = 0.12 \text{ s}$	Motor time constant
$\tau_{\text{sb}} = 0.2 \text{ s}$	Stabilizer bar time constant
$K_{\text{a}} = 6.4267$	Feed-forward gain of the headlock gyro system
$K_{\text{P}} = 0.667/K_{\text{a}}$	Proportional feedback gain of the headlock gyro system
$K_{\text{I}} = 0.713/K_{\text{a}}$	Integral feedback gain of the headlock gyro system

constraints and reasonable initial values (on-axis values from Sect. 49.4.2 and off-axis values as zeros), CIFER helps to search for optimal numerical solution based on frequency response matching. A stable result with good matching is obtained as follows:

$$
\begin{pmatrix} \dot{p} \\ \dot{q} \\ \dot{a}_{\text{up}} \\ \dot{b}_{\text{up}} \end{pmatrix} = \begin{bmatrix} -17.19 & 0 & 0 & 934.1 \\ 0 & -5.360 & 291.3 & 0 \\ 0.2745 & -0.49 & -5 & 0 \\ -0.49 & -0.2745 & 0 & -5 \end{bmatrix} \begin{pmatrix} p \\ q \\ a_{\text{up}} \\ b_{\text{up}} \end{pmatrix} + \begin{bmatrix} -102.48 & -38.08 \\ -11.73 & 31.95 \\ 0 & 0 \\ 0 & 0 \end{bmatrix} \begin{pmatrix} \delta_{\text{ail}} \\ \delta_{\text{ele}} \end{pmatrix}.
$$
(49.71)

With this numerical result, Figs. 49.19–49.22 show the corresponding comparison of frequency response between the data collected via actual flight tests and the CIFER derived model fit. For both the on-axis and off-axis responses, the matching is very good, indicating a high-quality identification result. Next, by comparing Eqs. 49.70 and 49.71, all the parameters involved in angular rate and rotor flapping dynamics can be finalized. Table 49.7 shows the identification results that have been obtained via flight test. Till now, all unknown parameters in the fixed-pitch coaxial model have been identified.
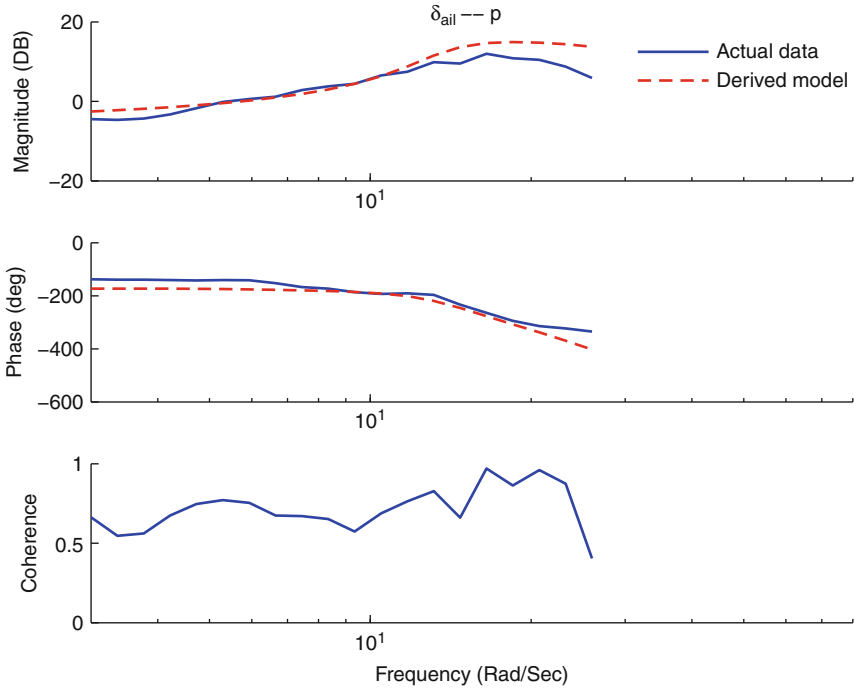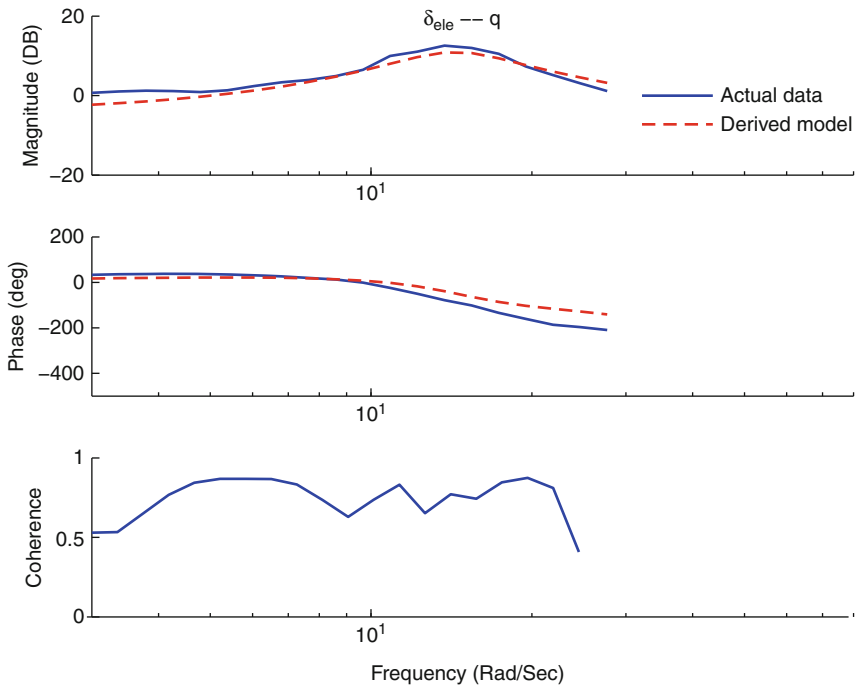
Fig. 49.19 Response comparison using frequency-sweep input ($\delta_{lat} - p$)
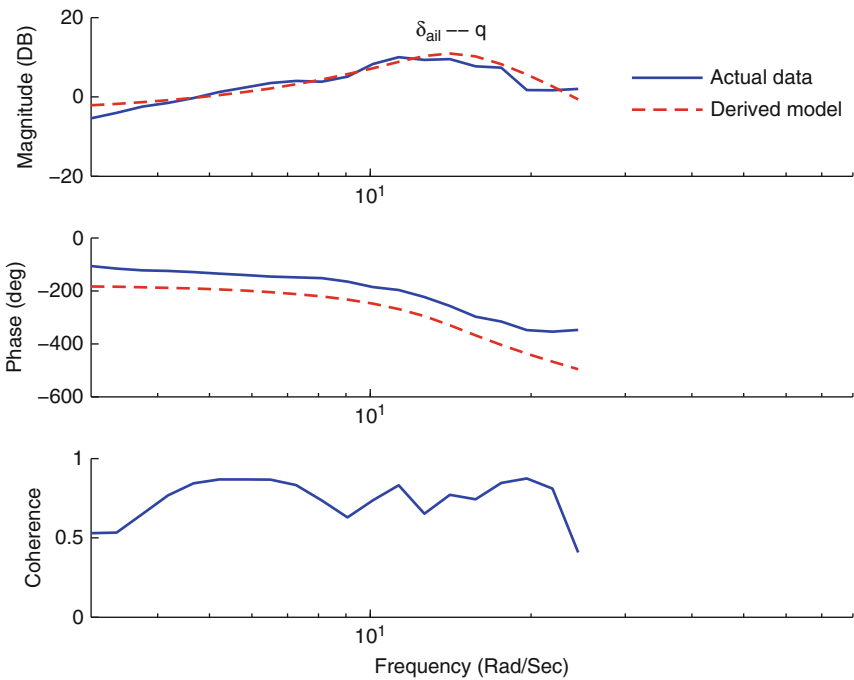
Fig. 49.20 Response comparison using frequency-sweep input ($\delta_{lat} - q$)
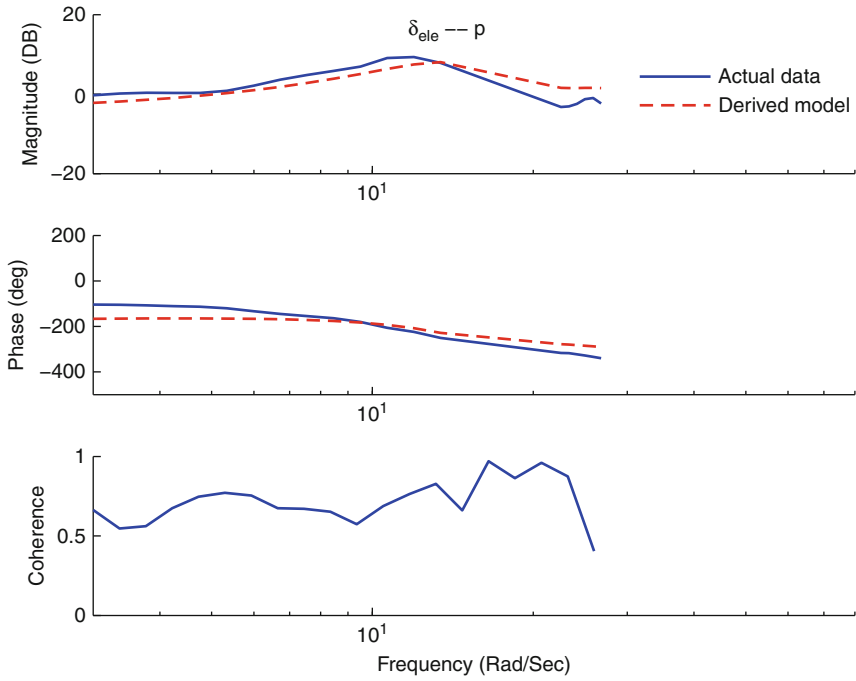
Fig. 49.21 Response comparison using frequency-sweep input ($\delta_{ele} - q$)

Fig. 49.22 Response comparison using frequency-sweep input ($\delta_{ele} - p$)

**Table 49.7** Parameters determined via flight test and CIFER

| Parameter	Physical meaning
$A_{a,\text{up}} = 0.4900$ rad s^{-1}	DC gain from stabilizer bar pitching angle to upper rotor longitudinal flapping angle
$B_{b,\text{up}} = 0.4900$ rad s^{-1}	DC gain from stabilizer bar rolling angle to upper rotor lateral flapping angle
$A_{b,\text{up}} = -0.2745$ rad s^{-1}	DC gain from stabilizer bar rolling angle to upper rotor longitudinal flapping angle
$B_{a,\text{up}} = 0.2745$ rad s^{-1}	DC gain from stabilizer bar pitching angle to upper rotor lateral flapping angle
$A_{a,\text{dw}} = 0.1217$ rad s^{-1}	DC gain from elevator input to lower rotor longitudinal flapping angle
$B_{b,\text{dw}} = -0.1217$ rad s^{-1}	DC gain from aileron input to lower rotor lateral flapping angle
$A_{b,\text{dw}} = -0.0450$ rad s^{-1}	DC gain from aileron input to lower rotor longitudinal flapping angle
$B_{a,\text{dw}} = -0.0450$ rad s^{-1}	DC gain from elevator input to lower rotor lateral flapping angle

49.5   Model Verification

It is always a good practice to verify a derived system model with actual input and output data. In this section, a comprehensive evaluation on the fidelity of the obtained nonlinear model of the ESky Big Lama (fixed-pitch coaxial helicopter) is shown. Four manual flight tests were carried out, which include:

1. Aileron channel perturbation with platform rolling left and right
2. Elevator channel perturbation with platform pitching forward and backward
3. Throttle channel perturbation with platform flying up and down
4. Rudder channel perturbation with platform yawing clockwise and anticlockwise

In each of these four flight tests, the pilot was asked to agitate only one of the four input channels. However, to make sure the helicopter position does not drift too much, minor off-axis inputs were also issued to lightly counter the cross-couplings between the channels. The time-domain results are shown from Figs. 49.23 to 49.26. Based on the recorded inputs, the transient response of the UAV attitudes, angular rates, and body-frame velocities are calculated by a MATLAB simulation program with the aforementioned nonlinear mathematical model (dashed lines in the figures). They are plotted together with the in-flight true data obtained by the onboard sensors (solid lines in the figures). The matching between the two is quite perfect. Note that for the roll and pitch angular rate dynamics, both the on-axis and the off-axis responses match very well, indicating a precise formulation of the coupling terms. Some minor mismatches are caused by the ignorance of high-frequency dynamics when formulating the model, especially for the motion of rotor flapping, which is theoretically highly complicated. Other discrepancies come from ground effect, wind disturbances, and measurement noises present in practical flight tests. In general, this is an accurate cross-coupled model for a fixed-pitch coaxial UAV with low maneuvering speed.
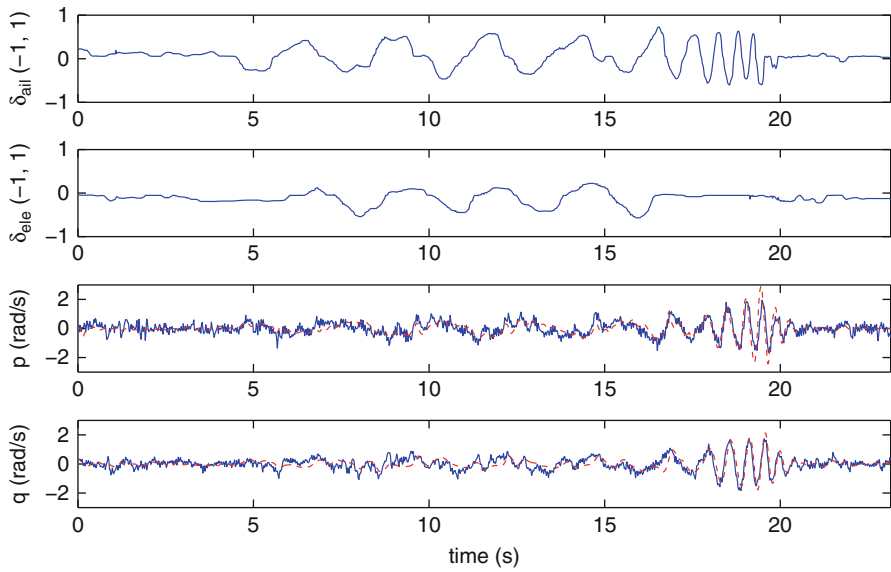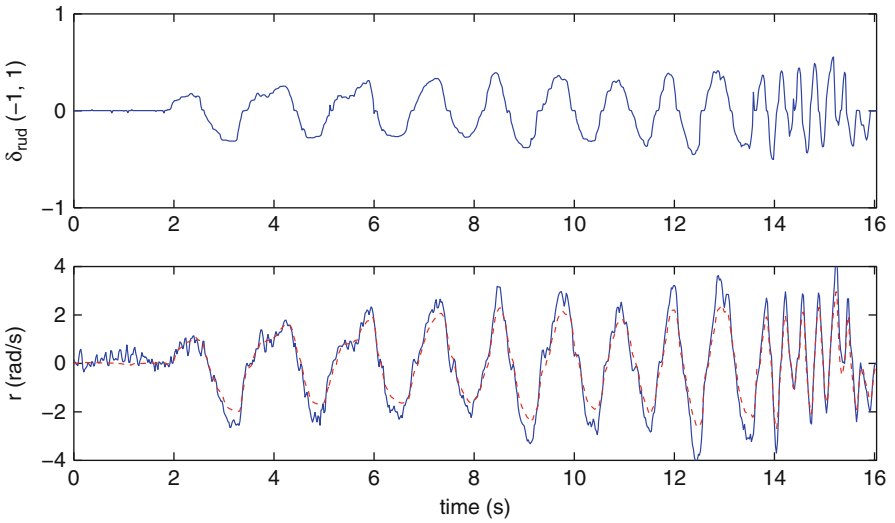
Fig. 49.23 Responses from aileron input perturbation
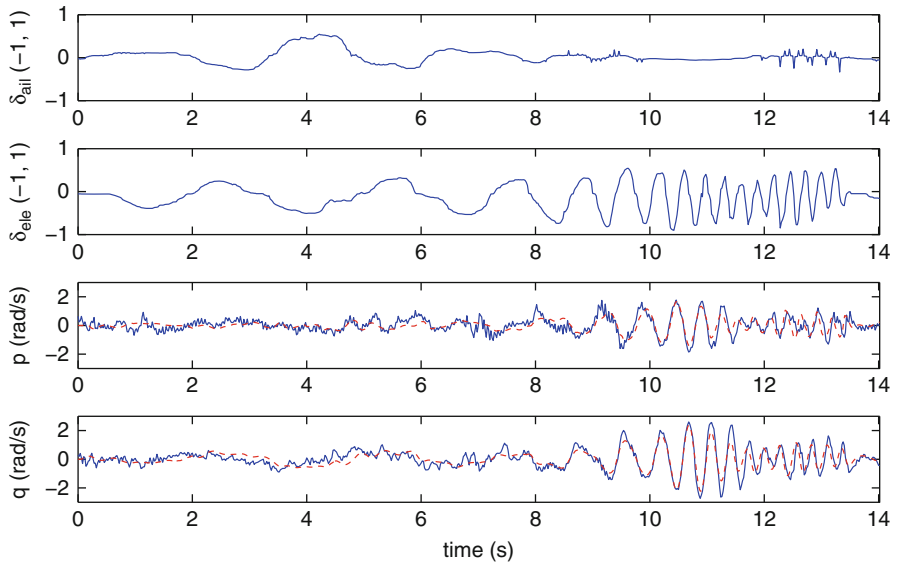
Fig. 49.24 Responses from elevator input perturbation
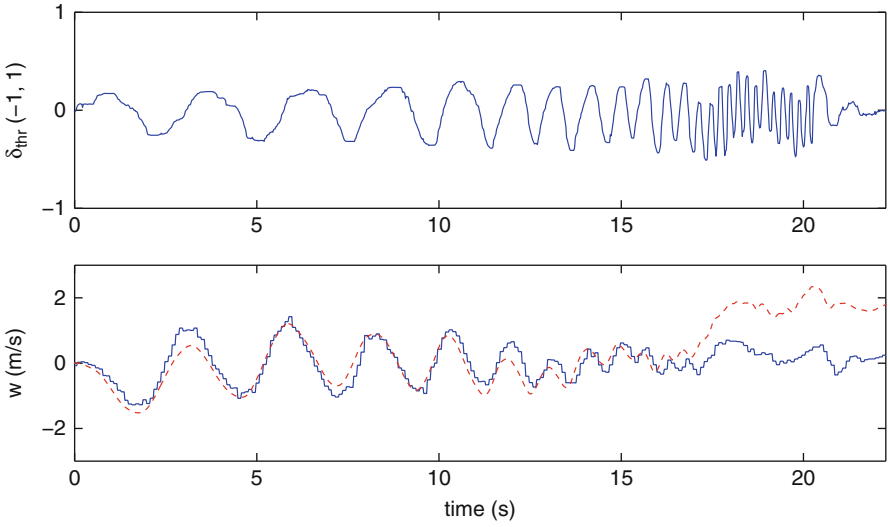
Fig. 49.25 Responses from throttle input perturbation

Fig. 49.26 Responses from rudder input perturbation

49.6   Conclusions

This book chapter has demonstrated the main procedures and challenges in modeling flight dynamics of aerial vehicles for the purpose of UAV development. By using the fixed-pitch and variable-pitch coaxial helicopters as examples, the model formulation, parameter identification, and model verification methods are explained in sequence with an adequate level of complexity for people with general engineering backgrounds.

For the model formulation, all analysis starts from the general working principle and model structure of the targeted systems. Formulas to describe the 6DoF kinematics and rigid-body dynamics are listed, and they are universal to all other types of UAVs. The general composition of forces and torques exerted on the UAV fuselage is more or less the same for the fixed-pitch and variable-pitch coaxial helicopters. However, the detailed formulation of individual force and torque generation are different and thus explained separately.

For the model-based parameter identification, the identification methods are categorized into three types, namely, direct measurement, test bench experiments, and flight tests. The ESky Big Lama, belonging to the fixed-pitch coaxial helicopter, is chosen to be a case study to illustrate some useful test bench and flight test setups to determine the model parameters. After all, a nonlinear model of the ESky Big Lama flight dynamics is fully derived with all parameters identified.

Finally, model verification is done to prove the feasibility of the whole methodology. By comparing simulation data with the actual in-flight data, the fidelity of the derived nonlinear model is guaranteed. It is also worth noting that the derived model has been actually used in control law design for an indoor coaxial UAV, and good hovering performance has been achieved (Wang et al. 2012).

It is believed that with the proposed systematic modeling methodology, the readers will get insightful knowledge about UAV modeling and parameter identification. Hopefully, these methods can be utilized and applied to other types of aerial platforms, too. It is also welcomed that more detailed aerodynamic formulations and other innovative parameter identification methods can be shared in future and thus complement this work.

References

C. Bermes, Design and dynamic modeling of autonomous coaxial micro helicopters. Dissertation, Eidgenossische Technische Hochschule ETH Zurich, 2010, Nr. 18847

A.R.S. Bramwell, G. Done, D. Balmford, *Bramwell's Helicopter Dynamics*, 2nd edn. (Butterworth-Heinemann, Oxford, 2001)

G. Cai, B.M. Chen, T.H. Lee, *Unmanned Rotorcraft Systems*. Advances in Industrial Control Series (Springer, New York, 2011)

G. Cai, B.M. Chen, T.H. Lee, K.Y. Lum, Comprehensive nonlinear modeling of a miniature unmanned helicopter. J. Am. Helicopter Soc. **57**, 1–13 (2012)

C.P. Coleman, A survey of theoretical and experimental coaxial rotor aerodynamic research, NASA technical paper 3675 (1997)

Y. Deng, R. Tao, J. Hu, Experimental investigation of the aerodynamic interaction between upper and lower rotors of a coaxial helicopter. ACTA Aeronaut. ET Astronaut. Sin. **24**(1), 10–14 (2003)

C.M. Harris, *Shock and Vibration Handbook*, 4th edn. (McGraw-Hill, New York, 1996)

R.K. Heffley, M.A. Mnich, Minimum-complexity helicopter simulation math model, NASA technical report 177476 (1988)

W. Johnson, *Helicopter Theory* (Dover, Mineola, 1994)

H.W. Kim, R.E. Brown, Coaxial rotor performance and wake dynamics in steady and manoeuvring flight, in *American Helicopter Society 62nd Annual Forum Proceedings*, Phoenix, 2006, vol. 1, pp. 20–40

J.G. Leishman, *Principles of Helicopter Aerodynamics* (Cambridge University Press, Cambridge/ New York, 2006)

J.W. Lim, K.W. McAlister, W. Johnson, Hover performance correlation for full-scale and model-scale coaxial rotors. J. Am. Helicopter Soc. **54**(3):32005-1–32005-14 (2009)

B. Mettler, *Identification Modeling and Characteristics of Miniature Rotorcraft* (Kluwer, Norwell, 2002)

P. Mukherjee, S.L. Waslander, Modeling and multivariable control techniques for small coaxial helicopters, in *AIAA Guidance, Navigation, and Control Conference*, Portland, 2011. AIAA-2011-6545

D. Neamtu, R. Deac, R.D. Keyser, C. Ionescu, I. Nascu, Identification and control of a miniature rotorcraft Unmanned Aerial Vehicle (UAV), in *AQTR'10: Proceedings of the IEEE International Conference on Automation, Quality and Testing, Robotics*, Cluj-Napoca, 2010, pp. 1–6

K. Nonami, F. Kendoul, S. Suzuki, W. Wang, D. Nakazawa, Fundamental modeling and control of small and miniature unmanned helicopters, in *Autonomous Flying Robots*, ed. by K. Nonami et al. (Springer, Tokyo, 2010), pp. 33–60

O. Rand, V. Khromov, Aerodynamic optimization of coaxial rotor in hover and axial flight, in *27th International Congress of the Aeronautical Sciences*, Nice, 2010, pp. 1–13

A. Rosen, D. Seter, Vertical autorotation of a single-winged samara, in *Proceedings of the ASME Joint Applied Mechanics/Bioengineering Conference*, Ohio State University, Columbus, 16–19 June 1991

D. Schafroth, C. Bermes, S. Bouabdallah, R. Siegwart, Modeling and system identification of the muFly micro helicopter. J. Intell. Robot. Syst. **57**(1–4), 27–47 (2010)

M.K. Taylor, A balsa-dust technique for air-flow visualization and its application to flow through model helicopter rotors in static thrust, NACA technical note 2220 (1950)

S. Tsach, A. Tatievsky, L. London, Unmanned Aerial Vehicles (UAVs), in *Encyclopedia of Aerospace Engineering*, ed. by R. Blockley, W. Shyy (Wiley, Hoboken, 2010)

B. Wang, F. Wang, B.M. Chen, T.H. Lee, Robust flight control system design for an indoor miniature coaxial helicopter, in *Proceedings of the 10th World Congress on Intelligent Control and Automation*, Beijing, 2012, pp. 2918–2924